WICK-TYPE LIQUID-METAL COMBUSTION

ANNUAL REPORT

October 15, 1988 to October 14, 1989

·Prepared by

L.-D. Chen, H. Y. Lyu and K. Y. Hsu

The University of Iowa
College of Engineering
Department of Mechanical Engineering
Iowa City, Iowa 52242

October 1989

ABSTRACT

An experimental and theoretical investigation was conducted to study the wick combustion of Li and SF_6. A single-line laser induced fluorescence thermometry with Li_2 as fluorescence species was developed. The calibration experiments yielded promising results; refinements, however, are needed before the technique can be applied to combustion flame measurements. Wick combustion of ethanol and hexane in air as well as Li and SF_6 was conducted in a vacuum chamber at atmospheric and sub-atmospheric pressures. The ethanol and hexane wick diffusion flames showed flame oscillations, similar to flame flickers in buoyant jet diffusion flames. The oscillation frequency was estimated in the range 5 to 8 Hz at the pressures examined. The flame stand-off distance was found to increase when the system pressure was decreased. The wick combustion of Li and SF_6 resulted in a bright pinkish flame. The luminous zone appeared quite close to the wick surface at the condition examined. Near the "complete consumption" of lithium, the wick was burned out due to loss of liquid lithium as a heat sink. On the analysis, a conserved scalar approach was employed to model the wick flame. A single equation was obtain to describe the interface condition of the wick combustion. Numerical solutions were obtained for laminar wick diffusion flames. The prediction yields similarity profiles for both ethanol-air and Li-SF_6 wick diffusion flames although non-similar governing equations were retained in the formulation. The flame stand-off distance was found to increase as the system pressure was reduced, in agreement with experimental observation. The effects on mass burning rates due to fuel composition variations were studied employing fuel-rich and product-rich liquids at 0.0035 MPa in the analysis. It was found that the product-rich fuel yields a much lower flame temperature; the mass burning rate, however, was higher than the pure lithium at 0.01 MPa. This is a result of the decrease in flame stand-off distance, yielding an increase in the heat transfer to the wick surface when a product-rich fuel was used. It is also noted that the product rich liquid has a lower specific enthalpy of gasification compared to fuel-rich liquids and pure lithium. The findings on fuel mass burning rates are interesting - suggesting that the wick configuration may achieve a higher fuel utilization than the submerged jet. The future work for the next report period was also discussed.

TABLE OF CONTENTS

LIST OF TABLES

LIST OF FIGURES

NOMENCLATURE

Symbol	Description
a_i	correlation coefficients, Eqs. 2-4
A	spontaneous emission rate
c	speed of light
Cp	specific heat
D	binary diffusion coefficient
E	energy
f	dimensionless stream function, Eq. 12
F	Boltzmann fraction
g	acceleration of gravity
g_i	degeneracy
h	enthalpy
h_{fg}	enthalpy of vaporization
H	plate height
k	thermal conductivity
L	enthalpy of gasification
Le	Lewis number
N	number density of photons
Pr	Prandtl number
Q	collisional quenching rate
R	universal gas constant
Sc	Schmidt number
T	temperature
u	streamwise velocity
v	cross-stream velocity

V	detected signal
W	laser-induced absorption/stimulated emission
x	streamwise distance
y	cross-stream distance
Y_i	mass fraction of species i
Z	mixture function
Z_{Tot}	total partition function
β	collection efficiency, Eq. 24
η	similarity variable, Eq. 15
κ	Boltzmann constant
μ	dynamic viscosity
ν	frequency
ω_i	source/sink term in Species Equation, Eq. 9
Ω_c	solid angle
Φ	fluorescence signal, Eq. 24
ξ	similarity variable, Eq. 15
ρ	density
ψ	stream function, Eq. 14
$\dfrac{d\sigma}{d\Omega}$	scattering cross-section

Subscripts

1	ground state
2	excited state
c	collective quantity
e	electronic
f	fluorescence

g	gas phase
l	liquid phase
lin	linear fluorescence model
r	rotational
s	solid phase
sat	saturated fluorescence model
v	vibrational
w	wall condition
∞	ambient condition

ACKNOWLEDGEMENT

I.   INTRODUCTION

1.1   General Statements of the Problem

A novel liquid-metal combustion system involving the reaction of lithium (Li) and sulfur hexafluoride (SF_6) is studied. The system is unique in that it has a high energy density and a high specific energy and that it yields condensed phase products under normal operation conditions. The high energy density and high specific energy satisfy the volume and weight requirements of propulsion applications and the condensed phase product provides a means of closed system operation as desired by deep-sea propulsion vessels; thus the liquid-metal combustion system is ideal for undersea applications.

Two major system configurations have been identified, i.e. the submerged jet and the reactive heat pipe (or wick-type), e.g. see Hughes et al. (1983). The submerged jet was identified as a practical energy source for submersible vehicles (Parnell, 1987 and 1989); however, the material compatibility of lithium and the high temperature and condensed phase products of Li and SF_6 combustion makes detailed measurements of the flame structure extremely difficult in submerged jet combustors. The wick configuration, on the other hand, provides an optical access to study the combustion of Li and SF_6. The wick configuration also has intrinsic merits as an energy source for surface and under-sea propulsion systems.

When a wick was employed, liquid Li was supplied through the wick action and heat transfer was accomplished by evaporation and condensation of lithium (Hughes et al., 1983 and Faeth et al., 1978). The wick system was shown to operate at a lower power level but with a longer time duration compared to submerged jet systems. A submerged jet combustor requires direct injection of gaseous SF_6 into the liquid bath (Li) at under-expanded conditions. As a result, the injector was in contact with hot combustion products/lithium and the injector clogging and erosion becomes a problem which needs to be addressed. When the injector clogged, the oxidant flow was stopped and the combustion was terminated. Restart of a submerged-jet combustor, unfortunately, is very difficult. The wick combustor, on the other hand, can be designed free from injector clogging.

This was accomplished by confining the high temperature zones to a region away from the injector (Faeth et al., 1978). It was also noted (e.g., see You and Faeth, 1977) that the wick system can be designed to have a fast response to the load change, to be capable of system restart and to have flexible heat exchanger layout through the heat pipe operation.

1.2 Previous Related Investigations

A closed volume liquid-metal combustor utilizing Li and SF_6 as fuel and oxidant has been identified as an energy source for undersea propulsion applications. The liquid-metal combustion system is also known as the SCEPS system (Stored Chemical Energy Propulsion Systems), e.g. see Hughes et al. (1983) and can be operated independent of environmental conditions. The reaction of Li and SF_6 follows the stoichiometry:

$$8 \, Li + SF_6 \rightarrow 6 \, LiF + Li_2S \tag{1}$$

The combustion products (LiF and Li_2S) are soluble in liquid lithium, yielding two immiscible liquids: fuel-rich (or metal rich) and product-rich (or salt rich) liquids. The density of the product-rich liquid is heavier than the fuel rich liquid (and lithium as well), allowing for constant volume operations. A closed system operation based on liquid-metal combustion has been developed for undersea propulsion applications (Hughes et al., 1983 and Parnell, 1989).

As discussed earlier, two system configurations were proposed, e.g. see Faeth, et al. (1978) and Hughes, et al. (1983), the submerged jet and wick-type or reactive heat pipe combustors. A number of investigations relevant to the submerged-jet operation had appeared in the literature; for example, see Loth and Faeth (1989) and Parnell (1989) and references cited therein. Much less work, however, was reported for the wick-type liquid-metal combustion, despite the advantages over the submerged jet as an energy source for propulsion applications. The wick-type liquid metal combustion yields a gaseous diffusion flame near the wick surface as identified by Blakeslee

(1977). The reaction products, however, condensed as they convected and diffused to a low temperature region and eventually dissolved in the liquid bath to form two immiscible liquids (fuel-rich and product-rich liquids). A reactive heat pipe concept based on the wick operation was later developed and reported by You, et al. (1977), Alstadt and Faeth (1977), You and Faeth (1977). Faeth, et al. (1978) and Groff and Faeth (1978b). The fundamentals of wick-type liquid-metal combustion are not well understood; for example, the presence of non-condensible gases was found to drastically reduced the fuel mass burning rate (Blakeslee, 1977). The mechanism, however, was not understood. A better understanding of the mechanism can provide design guidance to reduce the non-condensible gas effects and provide guidance in system preparation.

1.3 Specific Objectives

As discussed, the wick-type liquid metal combustion has intrinsic merits as an energy source for surface and under-sea propulsion systems and the wick configuration can provide an optical access to study the combustion of Li and SF_6. The specific objectives of this project are: (1) to document the flame structure of wick-type Li and SF_6 combustion, (2) to obtain a better understanding of wick-type liquid-metal combustion, for example on the effects of fuel compositions on mass burning rates and (3) to develop prediction methods for wick combustion and to assess model predictability.

II. THEORETICAL CONSIDERATION

The basic phenomena of liquid-metal combustion were discussed in earlier studies; for example, the flowfield of submerged gaseous oxidant jets in liquid metal was discussed by Avery and Faeth (1975), Chen and Faeth (1983) and Loth and Faeth (1989) and the wick-type liquid-metal combustion was studied by Blakeslee (1977) and Faeth, et al. (1978). The combustion of a wick flame was found essentially a gaseous diffusion flame (Blakeslee, 1977) in which the fuel consumption rate was limited by the transport in the gas phase. To model the wick combustion of Li and SF_6, thermochemical properties of reactants and products were identified and the transport process was modeled.

2.1 Thermodynamic Properties of Li_2S

Thermochemical properties of reactants and products involved in Li-SF_6 combustion are generally available from JANAF Tables (Chase et al., 1985), except for Li_2S which were taken from Groff (1976). This was done by curve fitting Li_2S data reported by Groff (1976) to the format employed by the NASA code. The gas phase property was estimated from statistical thermodynamics based on spectroscopic data. Li_2S was assumed a simple harmonic oscillator and the frequency was estimated from similar molecules; in specific, H_2N, H_2O, H_2S, and Li_2O. The liquid and solid state properties were estimated from the properties of Na_2S, Li_2O, and Na_2O. Groff (1976) should be cons ted in estimating Li_2S properties. To utilize the NASA equilibrium program (CEC), we need to provide specific heat, enthalpy and entropy of Li_2S for inclusion in the data bank. This was done by curve fitting the Li_2S data of Groff (1976) to the format employed in the NASA code.

The specific heat correlations used in the NASA Code (CEC Program; Gordon and McBride, 1976) assumed the following form:

$$\frac{C_p}{R} = a_1 + a_2 T + a_3 T^2 + a_4 T^3 + a_5 T^4 \qquad (2)$$

The coefficients a_1, a_2, a_3, a_4 and a_5 were obtained by curve-fitting the specific heat data reported by Groff (1976). A least squares fit of fifteen temperatures, i.e., 300 K to 1600 K at 100 K increments and at the Li_2S normal melting point (1645 K), was made for solid phase specific heats, and 25 temperatures (1645 K and 1700 to 4000 K at 100 K increment) and 41 temperatures (1000 to 5000 K at 100 K increment) were used for the liquid-phase and gas-phase specific heats, respectively. The obtained correlation coefficients are summarized in Table 1.

Table 1. Coefficient for Li_2S Specific Heat Correlations

Coefficients	Solid	Liquid	Gas
a_1	0.56732404E+01	0.96966147E+01	0.70533838E+01
a_2	0.11686870E-01	0.11409415E-02	0.50293408E-03
a_3	-0.19245575E-04	-0.56692271E-06	-0.22771507E-06
a_4	0.16212627E-07	0.12559047E-09	0.46648819E-10
a_5	-0.47654715E-11	-0.10217635E-13	-0.35727596E-14
a_6	-0.61355396E+05	-0.57484191E+05	-0.23660173E+05
a_7	-0.26409861E+02	-0.44900746E+02	-0.11219699E+02

Two additional coefficients, a_6 and a_7, are also summarized in Table 1 which were used in the enthalpy and entropy correlations:

$$\frac{H}{RT} = a_1 + \frac{a_2}{2} T + \frac{a_3}{3} T^2 + \frac{a_4}{4} T^3 + \frac{a_5}{5} T^4 + \frac{a_6}{T} \tag{3}$$

$$\frac{S}{R} = a_1 \ln T + a_2 T + \frac{a_3}{2} T^2 + \frac{a_4}{3} T^3 + \frac{a_5}{4} T^4 + a_7 \tag{4}$$

The two coefficients, a_6 and a_7, were determined from the enthalpy integration (a_6) and from

Clausius-Claperyon equation (a_7). In arriving at the above values, the gas-phase enthalpy of formation was determined, from statistical mechanics, -178.06 kJ/mole at 298.15 K and 0.1 MPa. The liquid-phase enthalpy of formation was accordingly determined -451.55 kJ/mole at 298.15 K. The solid-phase enthalpy of formation was determined -492.91 kJ/mole at 298.15 K, based on heat of fusion 49.4 kJ/mole and liquid-phase enthalpy -337.78 kJ/mole at the normal melting point.

2.2   Flow Analysis

The wick flame was assumed a diffusion flame with infinitely fast reactions and boundary-layer approximations were invoked. The major assumptions are

- Steady-state two-dimensional boundary layer flow.

- Chapman gas, unity Lewis number, constant Prandtl number and binary diffusion system.

- No radiative heat loss and negligible viscous dissipation.

- Infinitely fast chemical reactions and local equilibrium established in the flow

- Uniform interface condition.

Based on the above assumptions, a conserved scalar approach can be applied (Williams, 1985). The governing equations of conservation of mass, momentum, energy and species are

Continuity

$$\frac{\partial(\rho u)}{\partial x} + \frac{\partial(\rho v)}{\partial y} = 0 \tag{5}$$

Momentum

$$\rho u \frac{\partial u}{\partial x} + \rho v \frac{\partial u}{\partial y} = \frac{\partial}{\partial y}\left(\mu \frac{\partial u}{\partial y}\right) + g\,(\rho_\infty - \rho) \tag{6}$$

Mixture Fraction

$$\rho u \frac{\partial Z}{\partial x} + \rho v \frac{\partial Z}{\partial y} = \frac{\partial}{\partial y}\left(\rho D \frac{\partial Z}{\partial y}\right) \tag{7}$$

where the coordinate system is summarized in Fig. 1 and the mixture faction, Z, is a Shvab-Zeldovich variable, combining the energy and species equations. The energy and species equations are

Energy

$$\rho u \frac{\partial h}{\partial x} + \rho v \frac{\partial h}{\partial y} = \frac{\partial}{\partial y}\left(\frac{k}{Cp}\frac{\partial h}{\partial y}\right)$$

(8)

Species

$$\rho u \frac{\partial Y_i}{\partial x} + \rho v \frac{\partial Y_i}{\partial y} = \frac{\partial}{\partial y}\left(\rho D \frac{\partial Y_i}{\partial y}\right) + \omega_i$$
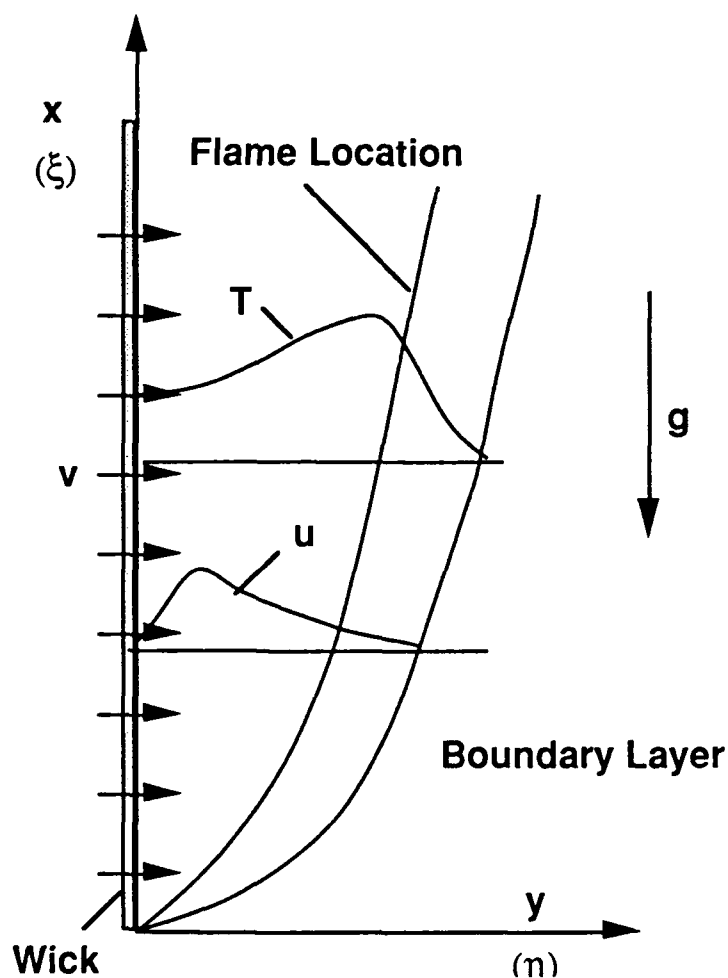
(9)

Figure 1. Coordinate System

where h is the total enthalpy, including enthalpy of formation, and Y_i is the mass fraction of species i and ω_i is the source/sink term due to chemical reactions. The governing equations were further cast into a dimensionless form in terms of stream function and similarity variables (Chen and Faeth, 1982). The transformed equations are

Momentum

$$\frac{\partial}{\partial \eta}\left(\frac{\rho\,\mu}{\rho_\infty\,\mu_\infty}\,f''\right) + 3\,ff'' - 2\,(f')^2 + \frac{\rho_\infty/\rho - 1}{\rho_\infty/\rho_w - 1} = 4\,\xi\left(f'\,\frac{\partial f'}{\partial \xi} - \frac{\partial f}{\partial \xi}\,f''\right) \qquad (10)$$

Mixture Fraction

$$\frac{\partial}{\partial \eta}\left(\frac{\rho\,\mu}{\rho_\infty\,\mu_\infty}\,\frac{1}{Pr}\,\frac{\partial Z}{\partial \eta}\right) + 3\,f\,\frac{\partial Z}{\partial \eta} = 4\,\xi\,(f\frac{\partial Z}{\partial \xi} - \frac{\partial f}{\partial \xi}\frac{\partial Z}{\partial \eta}) \qquad (11)$$

The continuity is automatically satisfied in the stream function formulation. The momentum equation employs a dimensionless stream function:

$$f(\xi,\eta) = \frac{\psi}{4\,\nu_\infty\,c\,(\xi H)^{1/4}} \qquad (12)$$

where

$$c = \left[\frac{g\,(\rho_\infty/\rho_w - 1)}{4\nu_\infty^2}\right]^{1/4} \qquad (13)$$

and the dimensional stream function ψ was defined as

$$\frac{\partial \psi}{\partial y} = \frac{\rho u}{\rho_\infty}, \quad \frac{\partial \psi}{\partial x} = -\frac{\rho v}{\rho_\infty}. \qquad (14)$$

The similarity variables are defined in the following

$$\xi = \frac{x}{H}, \quad \eta = cx^{-1/4} \int_0^y (\frac{\rho}{\rho_\infty}) \, dy; \tag{15}$$

The boundary conditions were specified to satisfy the non-slip wall and quiescent ambient conditions:

$$\eta = 0; \quad f = f_w, f' = 0, Z = 1, \text{ and}$$

$$\eta = \infty; \quad f' = 0, Z = 0. \tag{16}$$

To describe the interface thermodynamic state, a single equation was obtained for $Z = 1$. The equation is shown below

$$Y_{F,w} = 1 + \frac{1}{Le} \frac{L}{Cp_w} \frac{\left(\frac{\partial Y_F}{\partial Z}\right)_w}{\left(\frac{\partial T}{\partial Z}\right)_w} \tag{17}$$

where Le, L and Cp_w are respectively the Lewis number, enthalpy of gasification and specific heat at the interface. Equation (17) was obtained considering the conservation of mass and energy at the interface, i.e.

Mass

$$\rho_w v_w (1 - Y_{F,w}) = - \rho D \left(\frac{\partial Y_F}{\partial y}\right)_w \tag{18}$$

Energy

$$\rho_w \, v_w \, L = k \left(\frac{\partial T}{\partial y}\right)_w \tag{19}$$

The significance of Eq. (17) is that the interface condition is dictated by the flame structure within the context of the conserved scalar approach. Eq. (17) yields an interface fuel mass fraction is less than one under normal condition. This can be seen as the fuel vapor decreases and the temperature increases as Z is decreased (or moving away from the interface). It is noted that the interface fuel vapor mass fraction may approach unity near the mixture thermodynamic critical point at that condition the interface fuel mass fraction is equal to one.

2.3 Numerical Methods

As stated earlier, local equilibrium was assumed for the flow. The state relationship was constructed from the equilibrium calculation. The equilibrium calculation employed the NASA equilibrium code, i.e. NASA CEC Program by Gordon and McBride (1976). The CEC program utilized a Newton-Raphson iterative scheme in minimizing the Gibbs free energy to obtain equilibrium species and temperature.

The flow calculation employed a finite difference scheme (Keller box method) to obtain numerical solutions to the governing equations, Eqs. 10 and 11, at specified boundary and interface conditions, Eqs. 16 and 17. The numerical code was modified, allowing for wall blowing effects, from the computer program developed by Chen and Faeth (1982). The modified program was tested satisfactory for non-reactive flows (i.e., evaporative cooling) before adopting it for reactive flow computations.

III. EXPERIMENTAL CONSIDERATION

3.1 Apparatus

It is known that Li-SF$_6$ liquid-metal combustors were operated at sub-atmospheric pressures. Experiments were conducted in the vacuum chamber shown in Fig. 2 which was modified from a commercial product Vacuum/Atmospheres Model HE-133-5. The chamber was constructed with corrosion-resistant aluminum alloy (Type 6061), having an interior volume 0.43 m^3 (30" I.D. x 36" long) and equipped with an ante-chamber (0.044 m^3; 12" I.D. x 24" long).

The chamber interior design was illustrated in Fig. 3 in which a wick burner was placed inside. A stainless steel wick burner (316 Stainless Steel and 100x100 mesh) was placed inside the chamber. Different burner diameters (32 mm for Li-SF$_6$ and 25 mm for other experiments) and burner heights (25 to 89 mm) were used in the experiments. The wick screen was spot-welded on two stainless steel caps. An ANSI K-type (chromel-alumel) sheathed (stainless steel sheath) thermocouple was used to monitor the liquid bath temperature and a thermocouple indicator (Omega DP-80) was used for temperature readout. The thermocouple output was also interfaced with a Mac IIx work station using an A/D converter (National Instrument MIO-16-9). A stainless steel plate was placed above the burner to quench the hot plume rising from the wick burner. A well insulated (Cole Palmer N-03116-40) brass heater block (25 mm in diameter and 60 mm long) heated by nichrome wires (AWG Gauge 20) was placed below the wick burner and the heating was controlled by a Variac (Fisher Model 09-521-22) and monitored by a Watt meter (Ohio Samitronics EM-5). It required 150 W to heat the lithium inside the wick burner to a molten state (around 400 °C) prior to combustion experiments. Coiled nichrome wires (AWG Gauge 20) with a small lithium solid were used as the ignitor. The ignitor wire was heated by a Variac (Research LabVac 30-12).
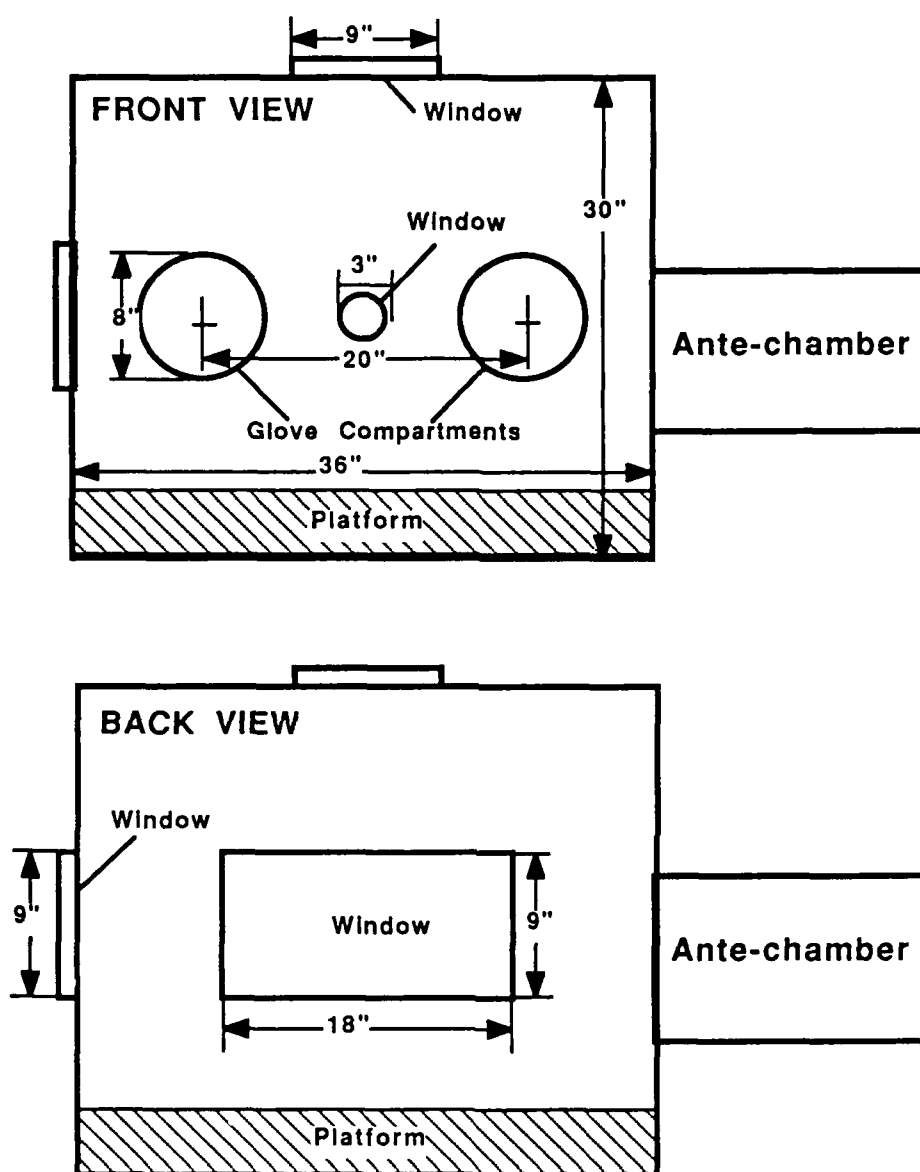
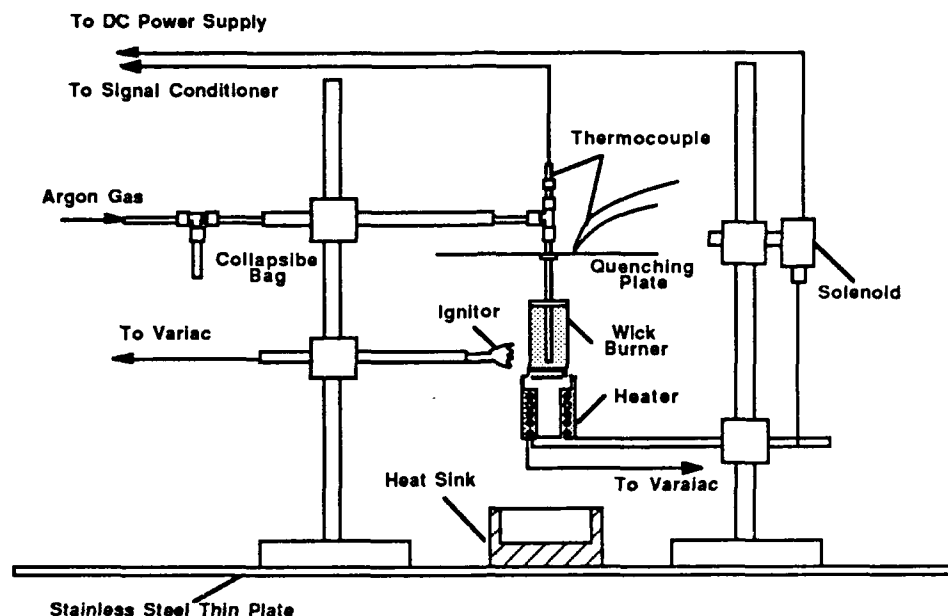Figure 2. Schematic of the Vacuum Chamber

Figure 3. Schematic of the Burner Arrangement

The gas supply to the chamber was illustrated in Fig. 4. To prepare the wick burner, the chamber was first evacuated to <0.2 torrs using a chemical pump (Alcatel Model 2020CP1) and back filled with the zero-gas grade argon gas (Matheson 99.998% purity) to atmospheric pressure. A "purge" argon gas (Air Products zero-gas grade, 99.99% purity) was also plumbed to the vacuum chamber intended for fast delivery of argon gas in case of emergencies. The pressure of the purge gas was regulated slightly above 0.1 MPa (1 atm). The chamber pressure was monitored by two vacuum gauges (Wika, -30"/30" Hg) and one pressure transducer (Wallace & Tiernan Model 66-100, 0.005 psia precision). High purity SF_6 (Matheson, Instrument Purity 99.99% purity) was used as oxidant and technical grade ^7Li (99.9 % purity, Lithium America; 12.7 mm lithium rods packed in mineral oil or argon gas) was used as fuel.

The lithium sample was cleaned with hexane and methanol and carefully prepared to obtain contamination free samples for combustion experiments. Prior to each experiment, the wick burner was cleaned with methanol and baked at low pressures (inside the vacuum chamber) to remove contaminants. The entire chamber (including the ante-chamber) was evacuated to <0.2 torr
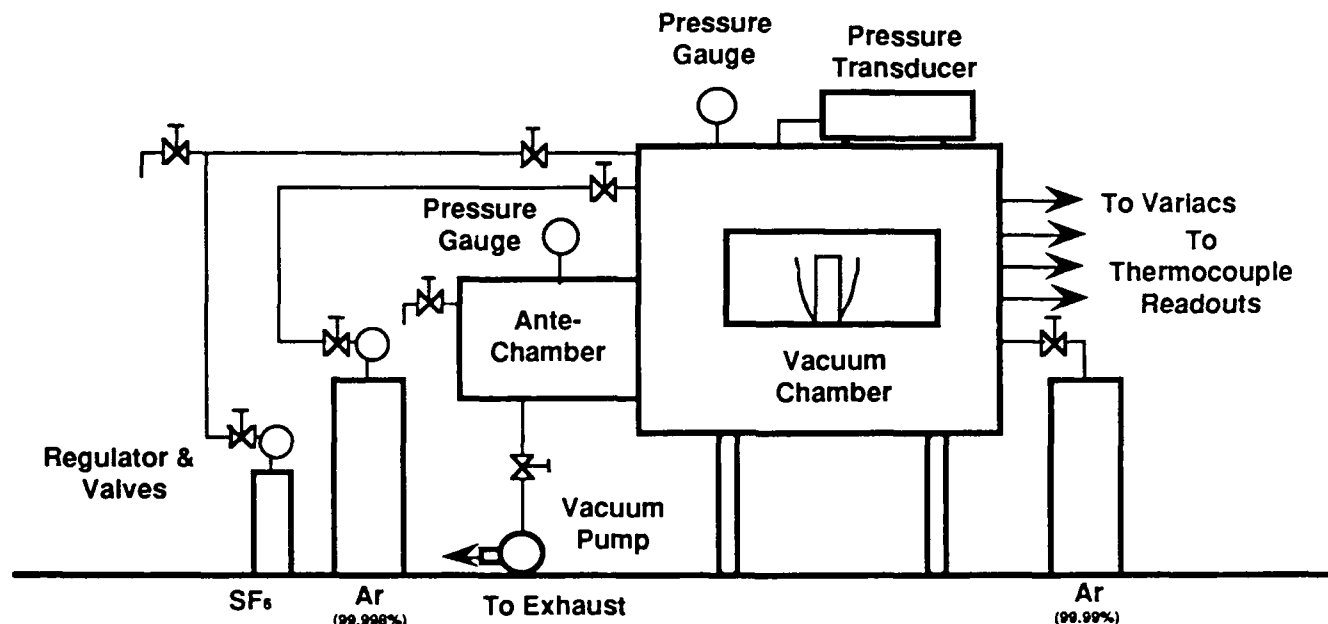
Figure 4. Gas Supply

and back-filled to one atmospheric pressure with argon gas. This step was repeated at least once.

The inner door of the ante-chamber was then closed manually (through the glove port). An

untreated lithium sample (covered with mineral oil) was placed inside the ante-chmaber through the

outer door of the ante-chamber. The ante-chamber was then evacuated and back-filled to one

atmospheric pressure with argon gas. The lithium sample was moved to the main chamber from

the ante-chamber through the inner door of the ante-chamber. Reagent grade Hexane (99.9 %

purity) was used to remove mineral oil from the lithium sample and methanol (Reagent Grade; 99.9

% purity) was used to remove hexane and oxidized layer from the lithium sample. Following the

preparation procedure outlined above, cleaned lithium samples were obtained. The cleaned lithium

sample was placed inside the wick burner. The chamber was evacuated and the lithium sample

was heated. The lithium sample was heated to 400 °C (or above) to wet the wick surface. The

chamber was then back-filled with SF_6 for subsequent combustion experiments. The combustion

process was monitored and recorded using a VHS format video camera (Panasonic WV3110-DX)

for subsequent review and analysis. A 35 mm camera (Canon AE-1) was used to take photographs of the video directly off a TV screen.

The optical arrangement of the diagnostics is shown in Fig. 5 in which a top view of vacuum
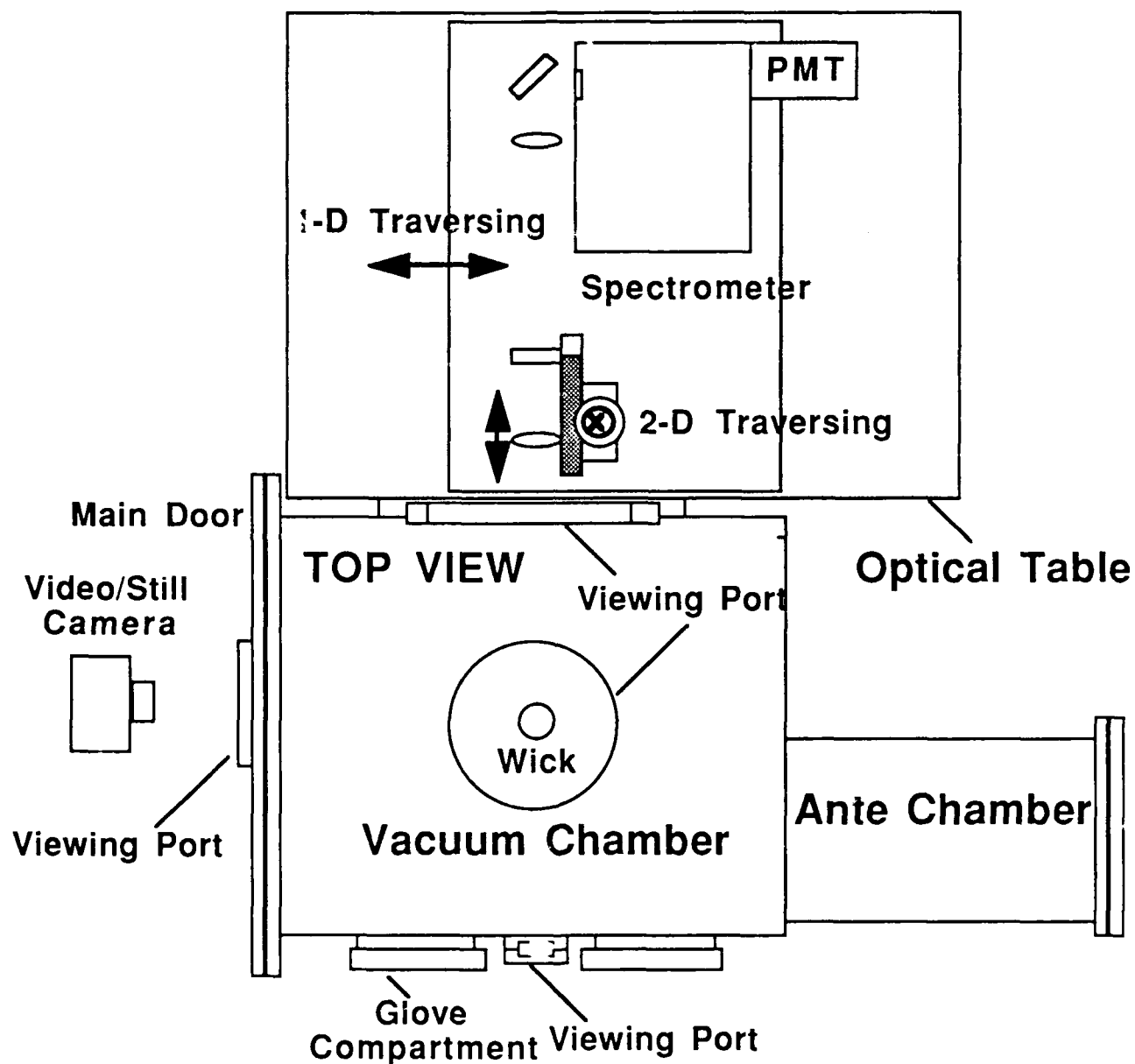

Figure 5. Experimental Set Up for Wick Combustion Diagnostics

chamber was illustrated. A three dimensional traversing mechanism which consists of linear bearings and uni-slides was designed, acquired (from commercial products) and assembled with in-house made components. The design provides a fixed optical axis (focusing lenses and spectrometer) for laser induced fluorescence (LIF) measurements; the variation in vertical heights was accounted for by a pair of periscopes. Similar to that employed in the layout of LIF measurements, another traversing mechanism was also designed and assembled for laser Doppler velocity measurements using a back scattering mode operation.

3.2 LIF Thermometry

To develop the laser induced fluorescence (LIF) thermometry using $^7Li_2$ (Lithium America, 99.9 % purity) as fluorescence species, experiments were conducted with the apparatus shown in Fig. 6. The major components of the apparatus include a heat-pipe oven, an argon-ion laser, optics and photodetectors. The heat pipe was configured with five arms. Each arm has an optical window at its end. The heat pipe was operated to maintain a uniform inside temperature and was used for LIF thermometry calibration experiments. The oven temperature was determined from thermocouples (ANSI K-type) located at the center of the heat pipe. In the experiments, the central portion of the heat pipe was electrically heated and the far end was water cooled to protect the windows from attack by Li vapor. In preparing calibration experiments, lithium was placed inside the heat pipe and followed by evacuation and heating to remove contaminants from lithium. Argon gas was introduced to confine Li vapor in the central portion of the heat pipe, to protect the window from direct contact with lithium vapor and to control the system pressure. Adjusting heater and vacuum pump operation, steady-state conditions of desired temperature and pressure can be reached for LIF thermometry experiments.

An argon ion laser (Coherent CR-6, 6 W) was used to excite $^7Li_2$. The coincidence lines of argon ion laser output and $^7Li_2$ spectrum are well-documented (e.g., Luh, Bahns and Stwalley, 1988), the values are summarized in Table 2. In the present study, the single line excitation was

Table 2. Fluorescence Lines of $^{7}Li_2$ Molecule Excited
by Argon Ion Laser (B-X Transitions)

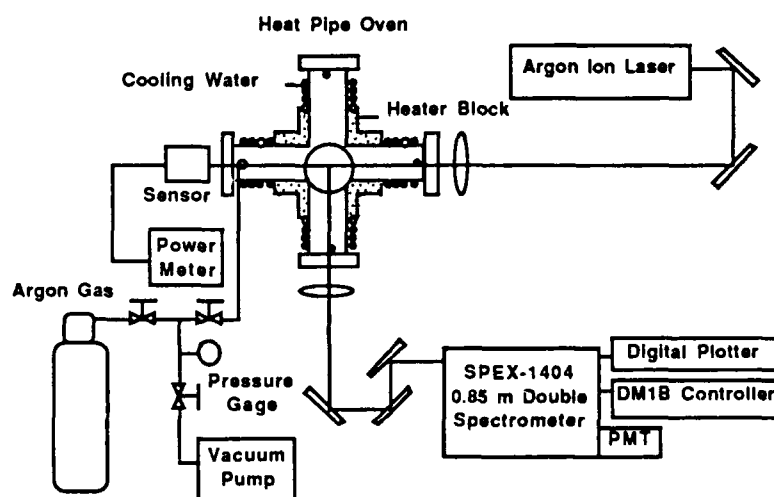| Laser Wavelength (nm)	B-X (v',J' - v",J")	LIF Wavelength (nm)
457.9	(9,9 - 2,8)	533.9-567.2
	(9,5 - 2,5)	550.3-564.9
472.7	(8,32-3,31)	550.0-568.6
476.5	(4,24-1,24)	525.1-551.0
	(9,61-2,62)	582.7-586.4
	(11,34-5,34)	551.0-588.9
488.0	(2,31-1,30)	514.7-540.7
	(6,45-3,46)	548.4-559.6
	(4,73-0,74)	552.3-564.7
	(9,19-6,18)	566.8-568.1
	(12,36-7,36)	584.1-591.3
514.5	(8,61-7,61)	574.6-582.1
	(3,30-5,29)	
	(9,38-9,37)	

Figure 6. LIF Thermometry Calibration Experimental Set Up

employed. In the discussion herein the temperature was obtained from a single line excitation (488 nm), assuming that the two closely-spaced fluorescence lines excited by a single-laser line have constant collection volume, detection efficiency and same quenching effects. The fluorescence signal was collected at a right angle from the excitation laser beam. A 0.85 m double spectrometer (SPEX-1404) was used to obtain the fluorescence spectrum. The height of the spectrometer entrance slit to was 20 mm and the width was adjusted in the range 20 to 50 μm to obtained good spectral resolutions. The measured fluorescence spectrum was analyzed, comparing with the theoretical spectrum. A Xe-lamp was used as reference to ensure the wavelength assignments.

To examine the fluorescence spectrum in a quantitative manner, the theoretical frequency and corresponding intensity distribution must be calculated from the theory to confirm the assigned fluorescence spectrum. The molecular constants of $B^1\Pi_u$ and $X^1\Sigma_+$ states of $^7Li_2$ were taken from Hessel and Vidal (1978) to calculate theoretical fluorescence line frequencies from specified excited states:

$$\nu = T'(v',J') - T''(v'',J'') + \Delta T'(v',J') \tag{20}$$

where ν is the fluorescence frequency resulting from the difference in term energies between the excited state $T'(v',J')$ and the ground state $T''(v'',J'')$. The ν and J are the vibrational and rotational quantum number of each respective state. The term energy of the excited B level (v',J') is

$$T(v',J') = \sum_{ij} A'_{ij} (v'+\frac{1}{2})^i [J' (J'+1) - 1]^j \tag{21}$$

and the corresponding term value of the ground state is given by

$$T(v'',J'') = \sum_{ij} A''_{ij} (v''+\frac{1}{2})^i [J'' (J''+1)]^j \tag{22}$$

The lambda-doubling $\Delta T'(v',J')$ of $B^1\Pi_u$ state is as follows

$$\Delta T'(v',J') = \delta \left(\sum_{lk} a'_{lk} \left(v'+\tfrac{1}{2}\right)^i (J'(J'+1)-1)^j \right) \tag{23}$$

where $\delta = 0$ for the Q series ($\Delta J = 0$) and $\delta = 1$ for P and R series ($\Delta J = \pm 1$). The Dunham-type molecular constants are denoted as A'_{ij}, A''_{ij} and a'_{lk} (Hessel and Vidal, 1978). The theoretical intensities of fluorescence spectrum were calculated following Luh (1985) in which a computer program known as Intensity (Zemke and Stwalley, 1984) was used to solve the Schrodinger equation for theoretical transition frequencies and the corresponding intensities.

In Li_2 LIF thermometry calibration, the 488.0 nm output of the Argon-ion laser was used as the excitation source. The resultant fluorescence spectrum is a collection of $^7Li_2$, $^6Li_2$ and $^7Li^6Li$ molecules. The fluorescence of $^7Li_2$ resulted in two stronger series from the excited states B(2,31) and B(6,45). The ratio of spectrally resolved fluorescence lines from B(2,31) and B(6,45) was used to obtain the temperature information. Two models, linear fluorescence and saturated fluorescence, were considered in analyzing the spectroscopy data. The measured fluorescence signal can be expressed as

$$\Phi = \beta\, \Omega_c\, V_c \left(\frac{d\sigma}{d\Omega}\right) N_j\, I_L \tag{24}$$

where β denotes the collecting efficiency, Ω_c the solid angle, V_c the collection volume, $\left(\frac{d\sigma}{d\Omega}\right)$ the scattering cross section, N_j the number density at the excited state and I_L the laser flux.

<u>Linear Fluorescence</u>. A three-level model was employed to describe the fluorescence signal resulting from transitions due to laser excitation. The linear fluorescence is

$$\Phi = \beta\, \Omega_c\, V_c\, h\, \nu_{jk}\, A_{jk}\, N_j \tag{25}$$

where h is the Planck's constant, v_{jk} and A_{jk} are the frequency and Einstein coefficient of the florescence transition between the excited state j and ground state k. The population of the excited state under the steady state assumption can be expressed as a function of absorption W_{ij}, Einstein coefficient A and quenching rate Q:

$$N_j = \frac{W_{ij}}{W_{ji} + A + Q} \tag{26}$$

The absorption W_{ij} is related to Einstein coefficient A_{ij}:

$$W_{ij} = \frac{2 B_{ij} I_L(v_{ij})}{\pi c \Delta v} \tag{27}$$

where Δv is the spectral width of the laser line and the absorption coefficient B_{ij} is defined as

$$B_{ij} = \frac{c^3}{8\pi h v_{ij}^3} A_{ij}. \tag{28}$$

The above equation was obtained assuming negligible quenching effects (Q = 0) which is typical at low pressures and negligible stimulated emission ($W_{ji} = 0$) compared to the absorption W_{ij}. In fact, the stimulated emission can be eliminated when the florescence signal was collected at a right angle from the laser beam. It was further assumed that the population follows a Boltzmann distribution, yielding a linear equation for fluorescence

$$\Phi_{lin} = (\frac{\beta \Omega_c V_c}{16\pi^3 c}) (\frac{I_L(v_{ij}) A_{ji} \lambda_{ij}^3}{\Delta v}) v_{jk} (\frac{A_{jk}}{\Sigma A_{jk}}) N_T \frac{g_j}{Z_{Tot}} \exp (\frac{hcE_i}{\kappa T}) \tag{29}$$

Where Δv is the laser spectral width, N_T the total number density of laser coupled states, g_j the degeneracy of the excited state $(2J_j + 1)$, Z_{Tot} the total partition function and E_i the energy of the

initial state.

Considering two fluorescence lines resulting from two different series excited by the same laser line, one can extract the temperature from the ratio of the two fluorescence signal Φ_{lin1} and Φ_{lin2}:

$$T = \frac{h\ c\ \Delta E}{K \ln \left(\frac{\Phi_{lin1}\ A_2\ \nu_2\ g_2\ I_L(\nu_2)}{\Phi_{lin2}\ A_1\ \nu_1\ g_1\ I_L(\nu_1)}\right)\frac{B_2}{B_1}} \tag{30}$$

where ΔE is the ground state energy difference (cm^{-1}) between the two fluorescences lines of different series. Since the laser intensity is likely to vary over the two excitation frequencies, ν_1 and ν_2, the difference in $I_L(\nu_1)$ and $I_L(\nu_2)$ must be considered when the linear fluorescence model is employed for temperature measurements.

Saturated Fluorescence. At saturated states, the fluorescence signal is independent of laser power and absorption coefficients. The saturated fluorescence signal is (Lucht, 1982):

$$\Phi_{sat} \alpha A_{jk}\ \nu_{jk}\ \frac{g_i\ g_j}{g_i + g_j}\ \exp\left(\frac{h\ c\ E_i}{\kappa\ T}\right) \tag{31}$$

where g_i and g_j are the degeneracies of the ground and excited states, respectively. The above equation also assumes negligible quenching effects. Taking the ratio of two saturated fluorescence line signals, $\Phi_{sat,1}$ and $\Phi_{sat,2}$, one obtains

$$T = \frac{h\ c\ \Delta E}{\kappa \ln \left(\frac{\Phi_{sat1}}{\Phi_{sat2}}\ \frac{A_2}{A_1}\ \frac{\nu_2}{\nu_1}\ \frac{\frac{g_{2i}\ g_{2j}}{g_{2i} + g_{2j}}}{\frac{g_{1i}\ g_{1j}}{g_{1i} + g_{1j}}}\right)} \tag{32}$$

where temperature is expressed in terms of ground state energy difference (ΔE), saturated fluorescence intensities (Φ_{sat}), frequencies (ν), Einstein coefficients (A) and degeneracies (g).

IV. RESULTS AND DISCUSSION

4.1 Experimental Results

LIF Thermometry. The fluorescence spectrum of $^7Li_2$ excited by an Argon ion laser at 488 nm was analyzed. The assignments of the spectrum were confirmed with theoretical calculations in terms of fluorescence-line wavenumbers and relative intensities. The spectral assignments are summarized in Tables 3 and 4 where λ is the wavelength in $\overset{\bullet}{A}$ and ω is the vacuum wavenumber. The comparison of relative intensity between experimental data and theoretical predictions was shown in Figs. 7 and 8. The uncertainty of intensity measurements can be improved by reducing the spectrometer scanning speed and spectrometer entrance slit width. Setting the scanning speed at 5 $\overset{\bullet}{A}$/s and the entrance slit at 25 μm, the measured fluorescence intensity at 507 °C was in good agreement with theoretical prediction, cf. Fig. 7. The measured fluorescence ratios of three different transition series in the temperature range 850 to 1050 K were compared to theoretical calculations. The experimental data were bounded by the calculations employing linear and saturated fluorescence models, Figs. 9-11. As can be seen the comparison is encouraging, the experimental data were found bounded by linear fluorescence and saturated fluorescence model calculations. Refinements, however, are needed to implement LIF thermometry techniques to combustion studies. In specific, the effects of excitation laser intensity on measured fluorescence signals need to be evaluated.

Wick Combustion. Prior to Li-SF$_6$ combustion experiments, the vacuum chamber was tested with combustion experiments of ethanol and hexane burning in the air. A vertical cylindrical wick (25 mm I. D. and 50 to 89 mm long) in which nonflammable fiberglass was packed was placed inside the chamber. The fiberglass was used to retain the liquid fuel inside the wick. Reagent grade ethanol (99.9 % purity) or hexane (99.9 % purity) was used. The wick combustion yields a non-luminous gaseous diffusion flame for ethanol at low pressures (0.03 and 0.05 MPa) and a luminous flame for ethanol and hexane at atmospheric pressure (0.1 MPa), e.g. see Figs. 12 and 13 for ethanol at 0.03 and 0.1 MPa and Fig. 14 for hexane at 0.1 MPa. The combustion

process can be divided in three stages: ignition, stable burning and extinction. After the ignitor was activated, a stable axisymmetric diffusion flame around the wick was established following a transient ignition stage. During the ignition stage, the flame spread over the wick surface, it usually started from the upper portion of the wick and propagated down to the leading edge of the cylinder. Near the fuel burn-out, the flame became unstable. Local extinction from the leading edge of the wick was seen, yielding an oscillating flame surface in longitudinal direction until extinction was observed.

Table 3. Assignment of $^7Li_2$ B(2,31) Fluorescence Excited at 488 nm

	R-BRANCH			P-BRANCH		
	Experiment		Theory	Experiment		Theory
v"	λ (A)	ω (1/cm)	ω (1/cm)	λ (A)	ω (1/cm)	ω (1/cm)
0	4800.25	20826.43	20826.11	4819.30	20744.11	20744.22
1	4879.95	20486.30	20486.52	4899.20	20405.80	20405.54
2	4960.90	20152.01	20152.24	4980.45	20072.91	20072.17
3	-	-	-	5083.30	19666.78	19744.15
4	5126.75	19500.10	19499.75	5147.55	19421.31	19421.55
5	5211.90	19181.52	19181.66	5232.90	19104.55	19104.41
6	5298.20	18869.09	18869.10	5319.55	18793.36	18792.82
7	5385.65	18562.70	18562.12	5407.80	18486.67	18486.86
8	5474.75	18260.60	18260.91	5497.05	18186.53	18186.82

Table 4. Assignment of $^7Li_2$ B(6,45) Fluorescence Excited at 488 nm

	R-BRANCH			P-BRANCH		
	Experiment		Theory	Experiment		Theory
v"	λ (A)	ω (1/cm)	ω (1/cm)	λ (A)	ω (1/cm)	ω (1/cm)
0	-	-	21576.66	-	-	21461.99
1	4705.50	21245.79	21244.67	4730.75	21132.39	21131.32
2	4778.95	20919.25	20918.06	4804.85	20806.49	20806.05
3	-	-	20596.88	4879.95	20486.30	20486.23
4	4929.15	20281.82	20281.20	4955.95	20172.14	20171.93
5	5005.75	19971.46	19971.11	-	-	19863.23
6	5083.30	19666.78	19666.67	5110.75	19561.15	19560.22
7	-	-	19368.00	-	-	19263.00
8	5240.80	19075.75	19075.19	5269.50	18971.86	18971.67
9	-	-	18788.36	-	-	18686.35
10	5401.60	18507.89	18507.64	5431.20	18407.02	18407.18
11	5483.05	18232.96	18233.17	5512.65	18135.06	18134.30
12	5564.75	17965.27	17965.10	5595.00	17868.14	17867.88
13	5646.45	17705.33	17703.62	5677.70	17607.88	17608.09

Relative Intensity of 7Li2 B(2,31)-X(v",30)

Relative Intensity of 7Li2 B(2,31)-X(v",32)
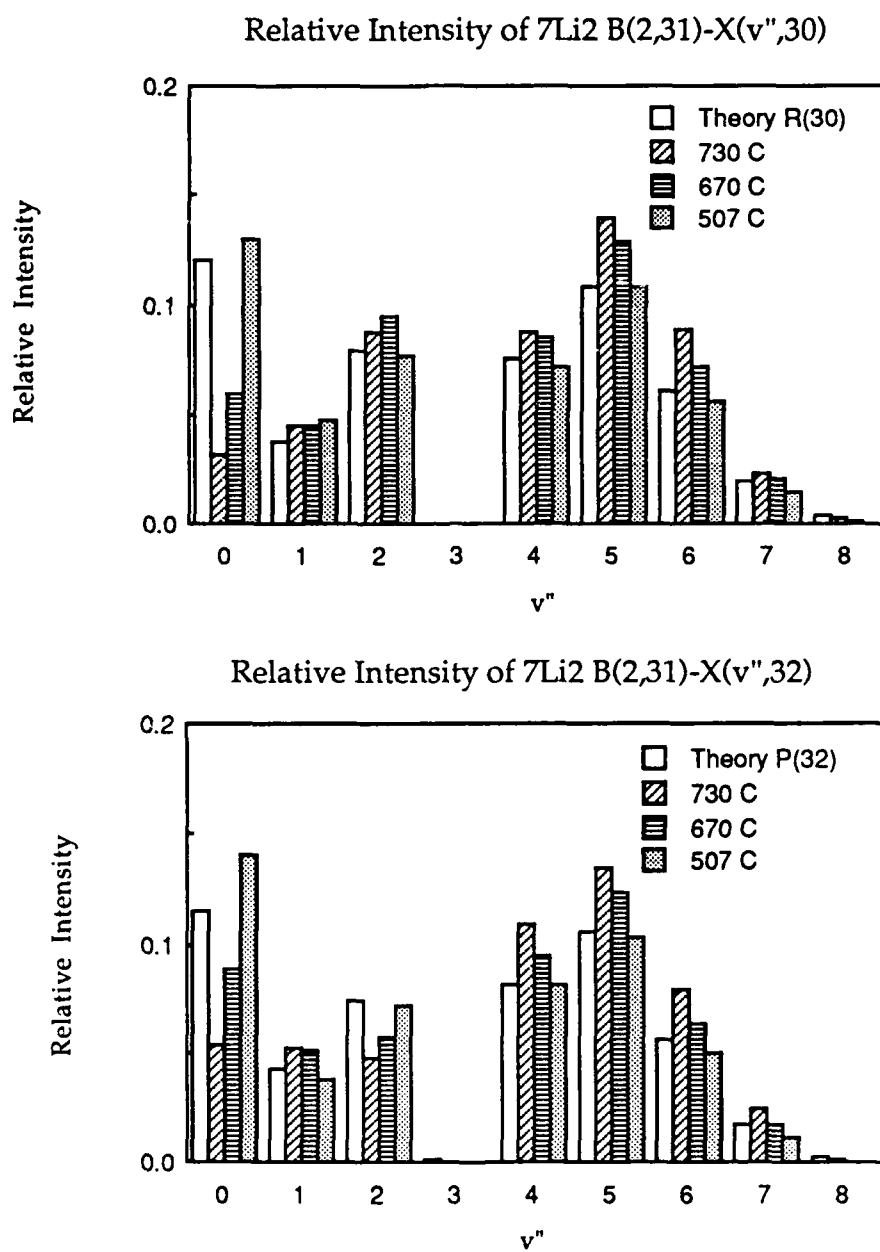
Figure 7. Relative LIF Intensity of $^7Li_2$ B(2,31) Excited at 488 nm.

Relative Intensity of 7Li2 B(6,45)-X(v",44) Excited by 488 nm
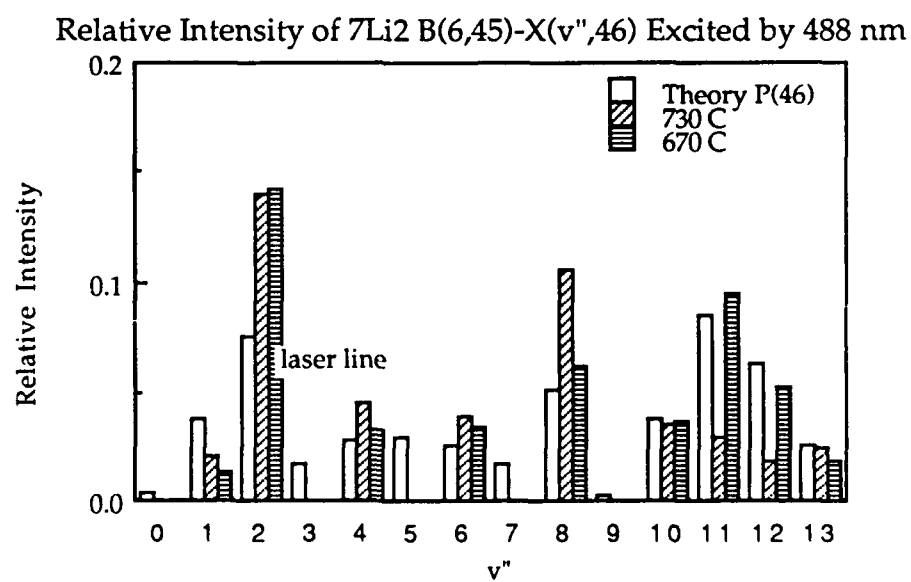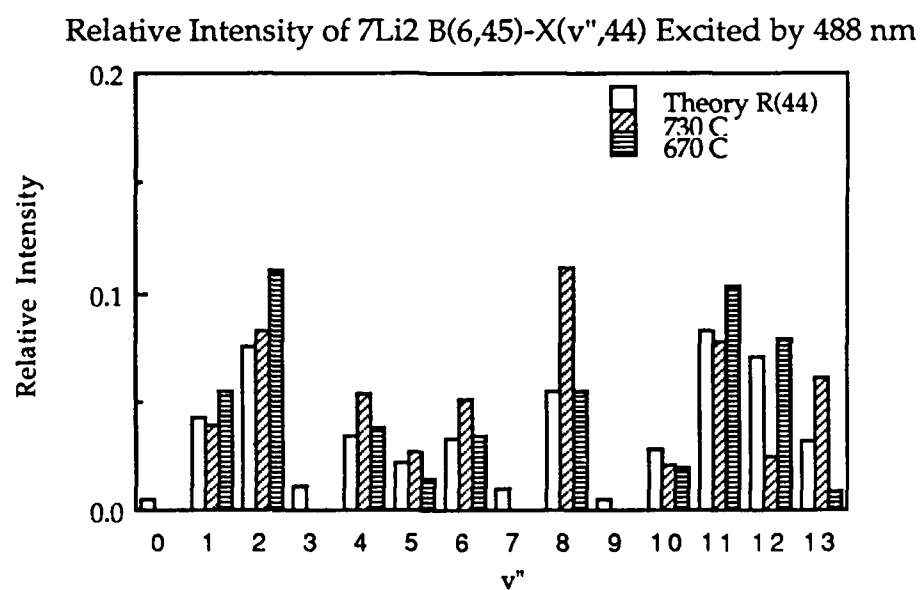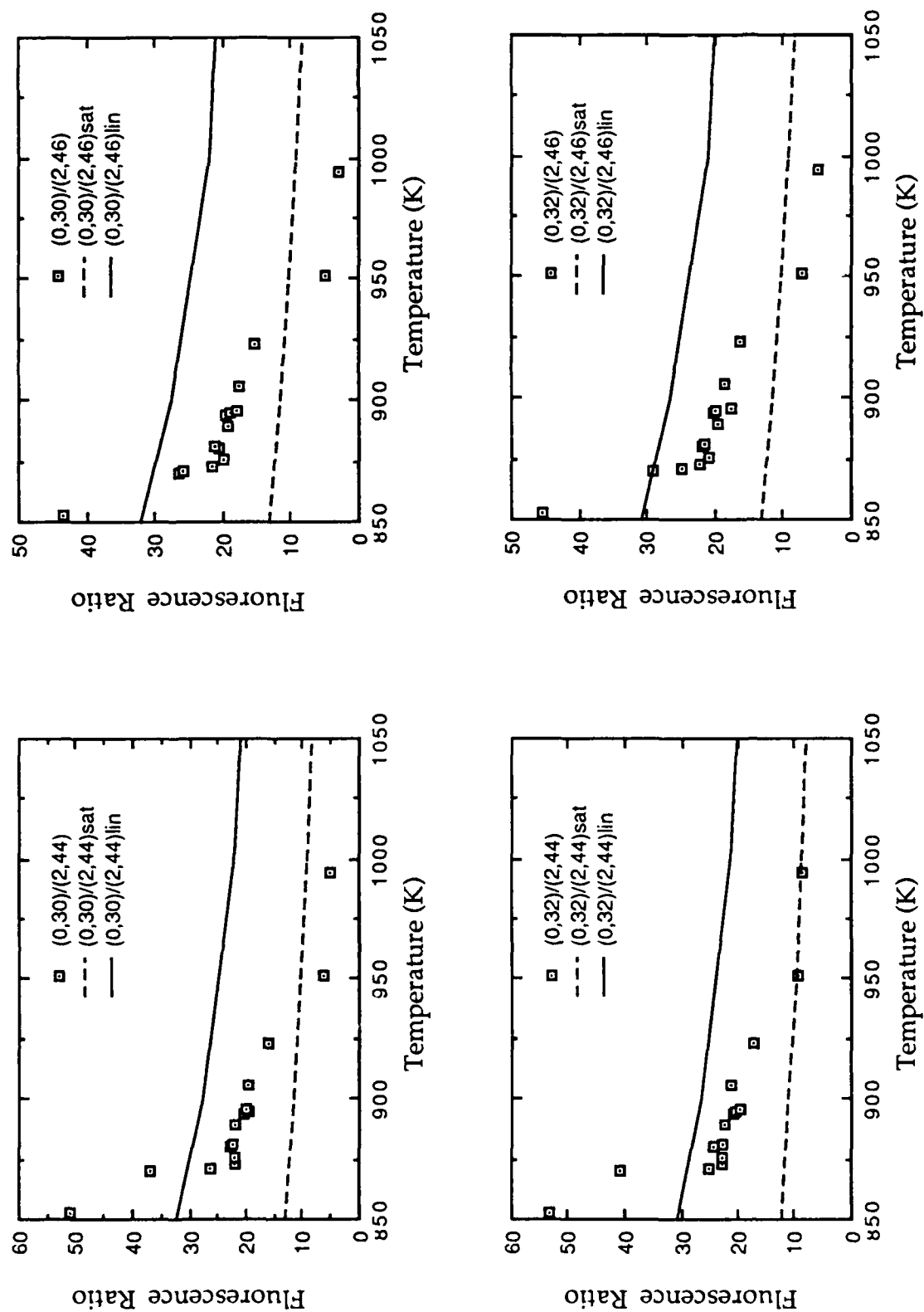

Relative Intensity of 7Li2 B(6,45)-X(v",46) Excited by 488 nm

Figure 8. Relative LIF Intensity of $^7Li_2$ B(6,45) Excited at 488 nm

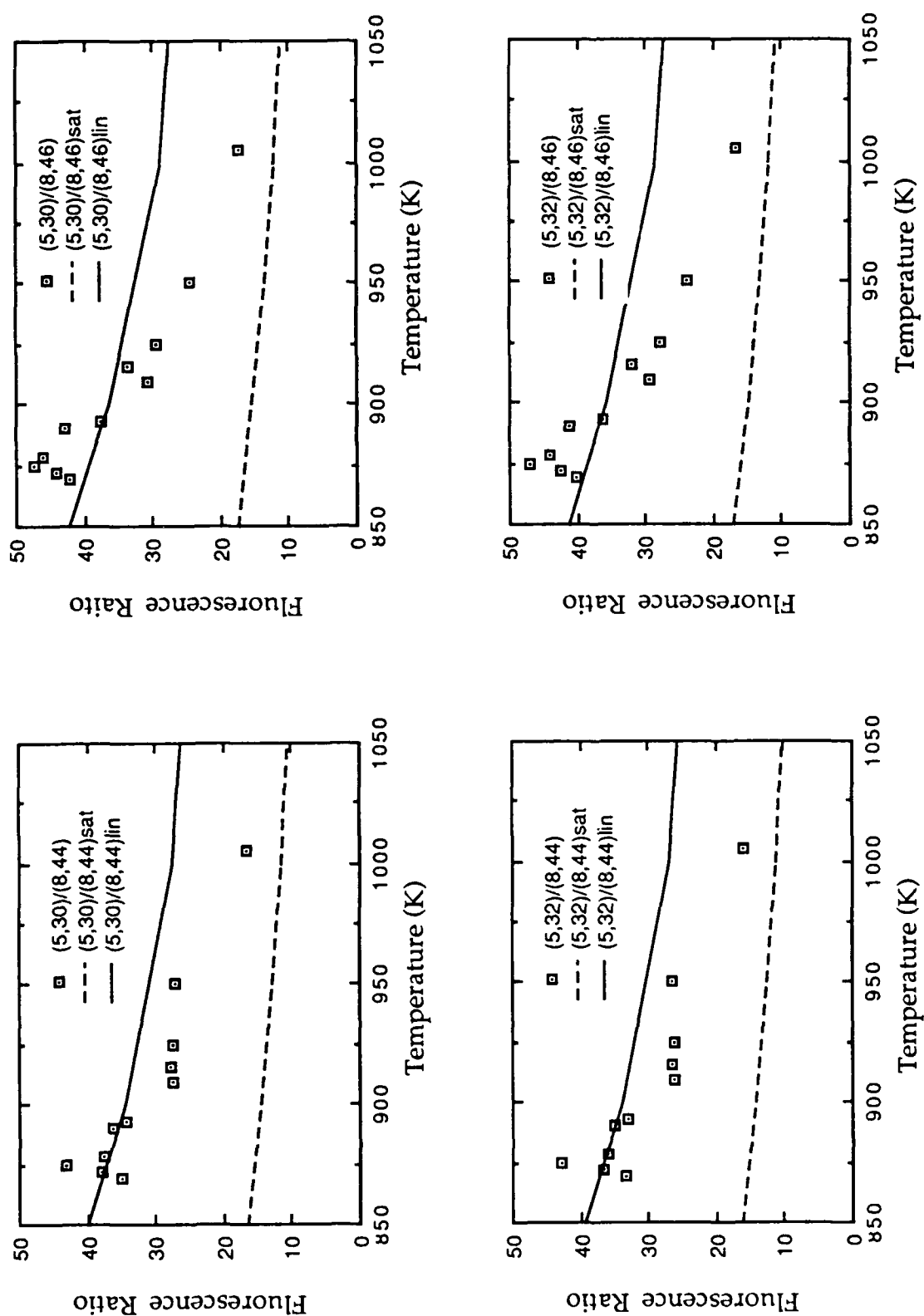Figure 9. LIF Thermometry Calibration of $^7Li_2$; B (2, 31)-X(0, 30/32)/B(6,45)-X(2,44/46)

Figure 10. LIF Thermometry Calibration of $^7Li_2$; B (2, 31)-X(5, 30/32)/B(6,45)-X(8,44/46)
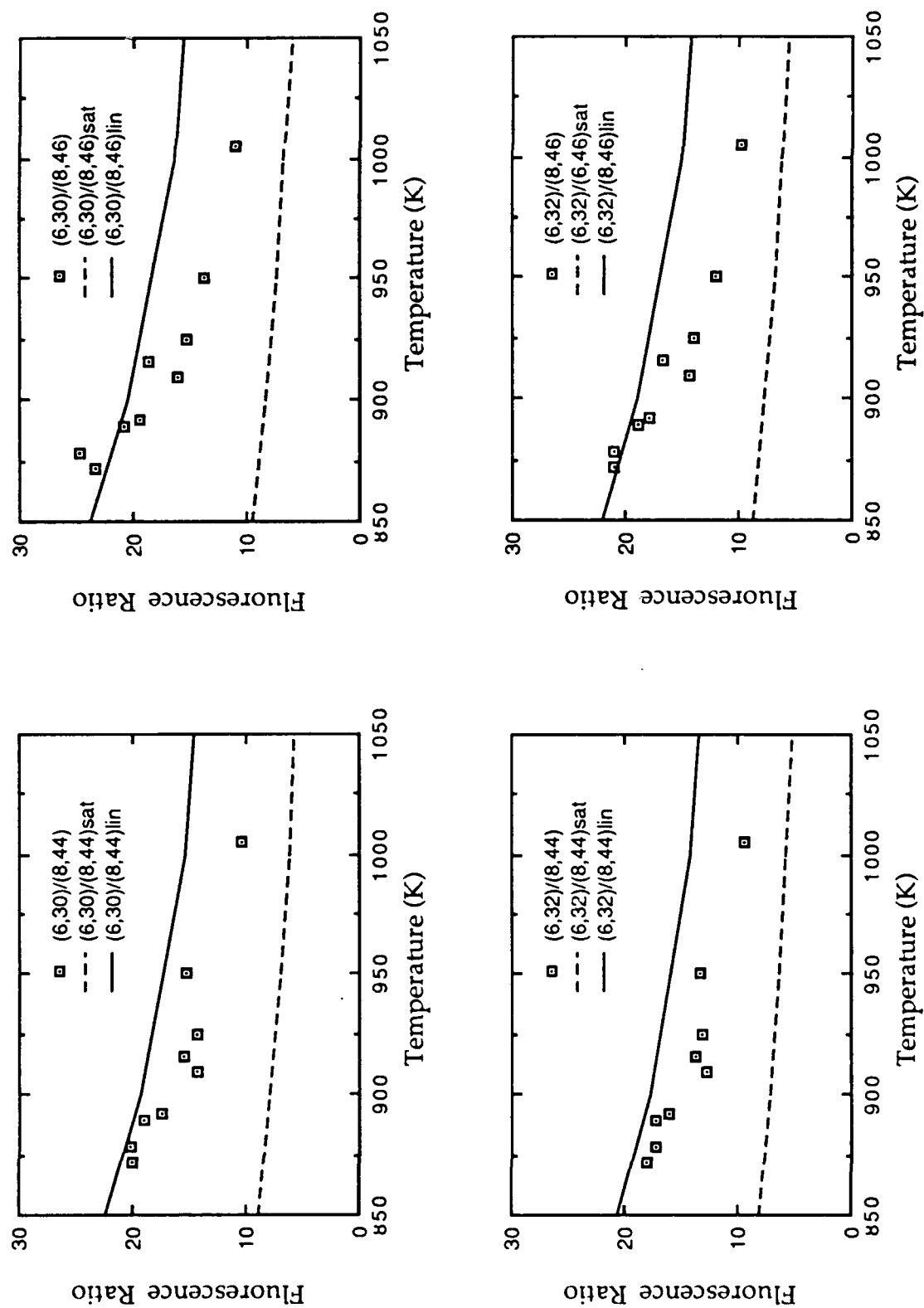
Figure 11. LIF Thermometry Calibration of $^7Li_2$; B (2, 31)-X(6, 30/32)/B(6,45)-X(8,44/46)

Spatial and temporal periodicities were observed in wick diffusion flames. The oscillation frequency was estimated in the range 5 to 8 Hz. The oscillation frequency of ethanol diffusion flames decreased when the system pressure was increased. Ethanol and hexane were found to have similar oscillation frequencies at 0.1 MPa. The spatial wavelength (e.g. 30 to 80 mm in the present experiments) increased as the system pressure was decreased. It is also noted that the oscillation in wick diffusion flames is similar to flame flickers in buoyant jet diffusion flames (Chen et al, 1989b), suggesting the existence of buoyancy driven vortical structures in a vertical boundary-layer diffusion flame. The flame stand-off distance increased as the system pressure was decreased (around 5 mm at 0.1 MPa and 10 mm at 0.03 MPa at a location 25 mm from the leading edge), in qualitative agreement with theoretical predictions.

Li-SF$_6$ Combustion. Combustion of lithium solids (in flake form, i.e. 2 to 3 mm thickness and 12 mm in diameter) in SF$_6$ (0.01 MPa) was successfully accomplished using Nichrome wires (AWG Gauge 20) as an ignitor. Following a transient stage (ejection of lithium) after the ignitor was activated, a very bright flame covered the lithium solid. A lithium "droplet" (molten lithium) was subsequently formed on the stainless steel plate inside the combustion chamber. Lithium was seen to wet the stainless steel (spreading on the surface in a dome or bell shape). The burning of the Li drop continued for a few seconds before before the extinction and solidification of the melt occurred. The sequential events of Li-solid combustion were summarized in Fig. 15.

Wick combustion of Li and SF$_6$ was studied. In the experiments conducted up-to-date, the chamber was filled with SF$_6$ at 0.01 MPa. The diameter of the wick was 32 mm and the height, excluding the end caps, was around 25 mm. Only one layer stainless steel screen was used to construct the wick cylinder. Heating the lithium to a temperature above 400 °C was necessary to wet the wick surface. A long nichrome wire coil (about 200 mm long) sided with the wick cylinder was used as the ignitor in the experiment shown in Fig. 16. Photographs shown in Fig. 16 were taken from the video at six different times after the ignitor was actuated, i.e. 2, 4, 17, 29, 32 and 33 seconds (cf. Fig. 16, from left to right and top to bottom). Once successful ignition was

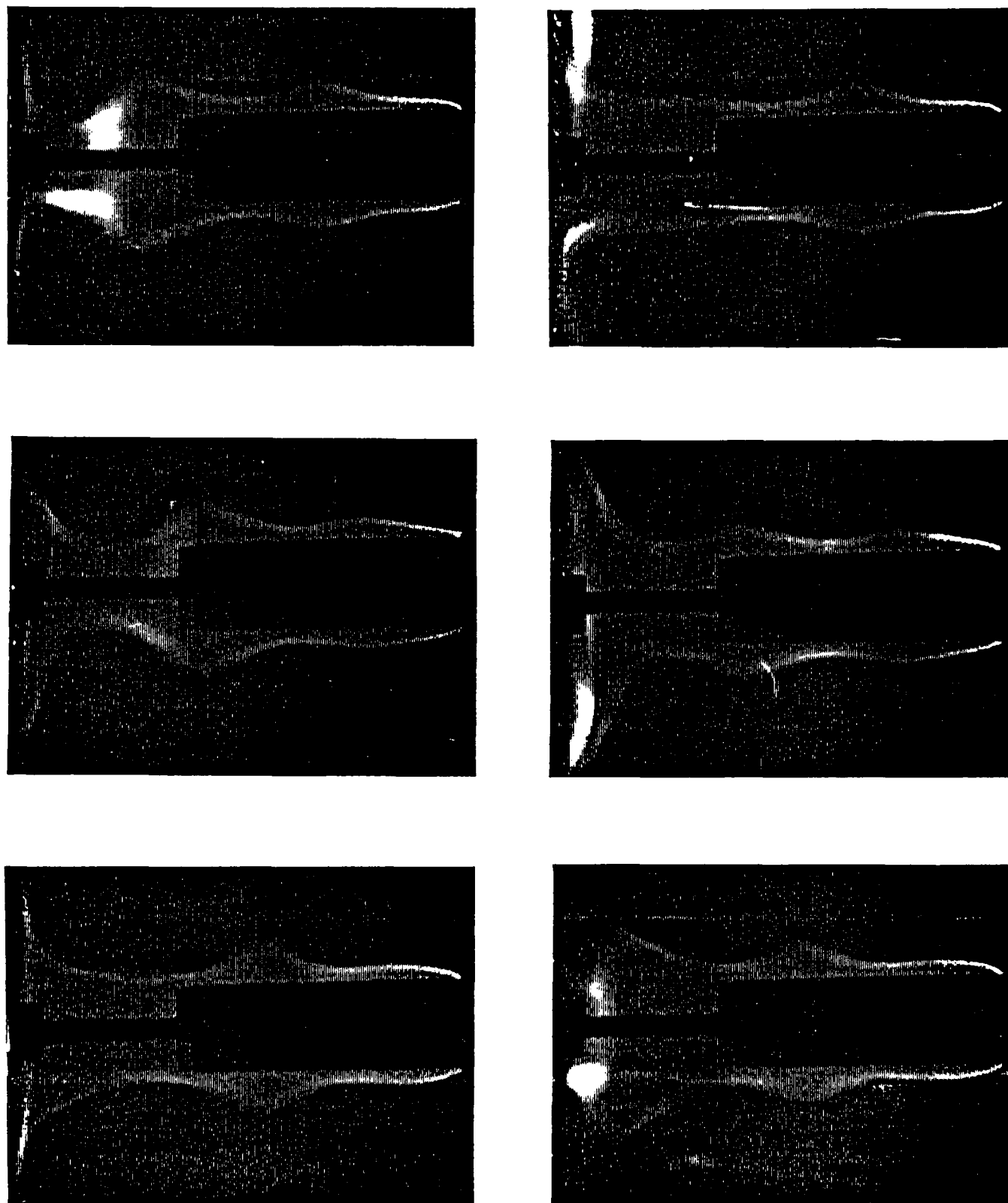Figure 12. Wick Combustion of Ethanol-Air at 0.03 MPa

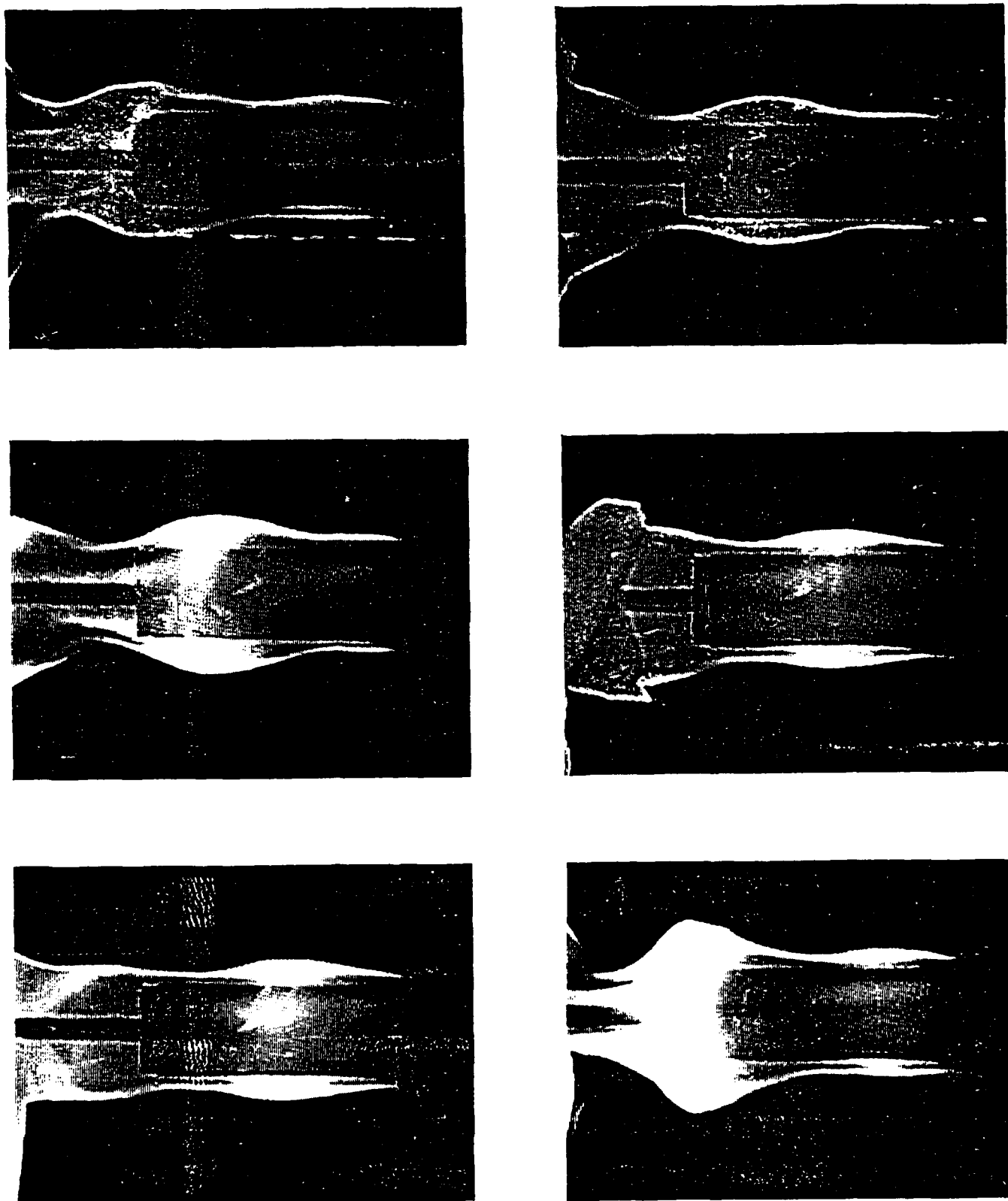Figure 13. Wick Combustion of Ethanol-Air at 0.1 MPa

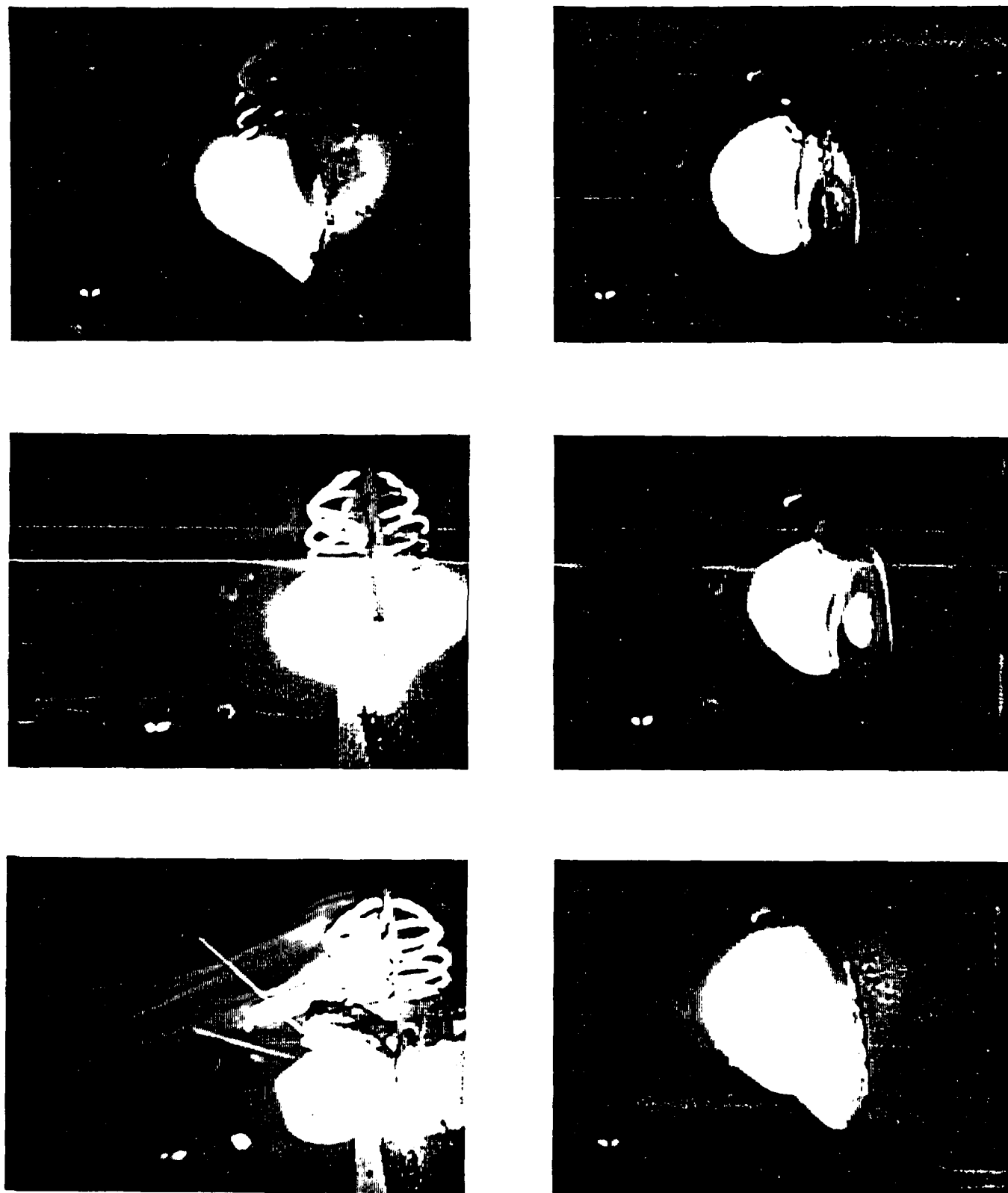Figure 14. Wick Combustion of Hexane-Air at 0.1 MPa
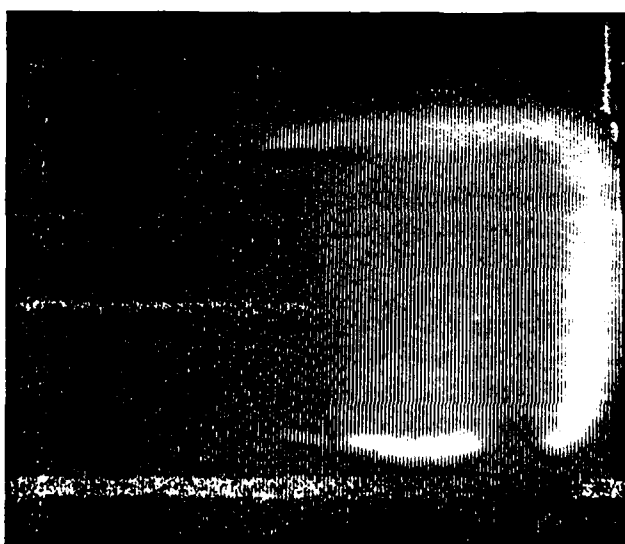
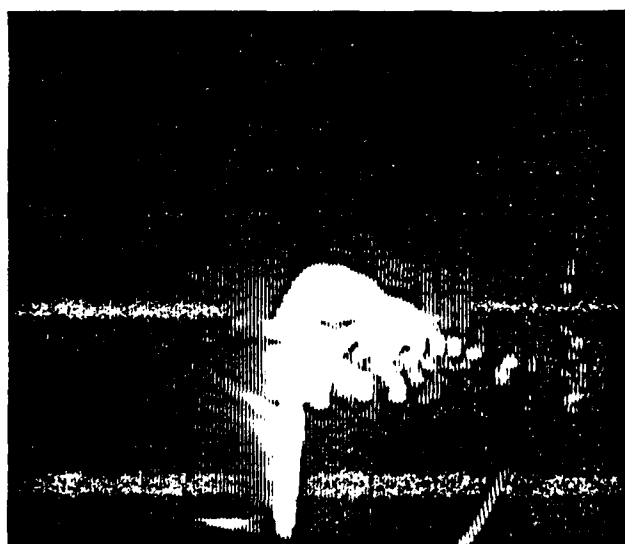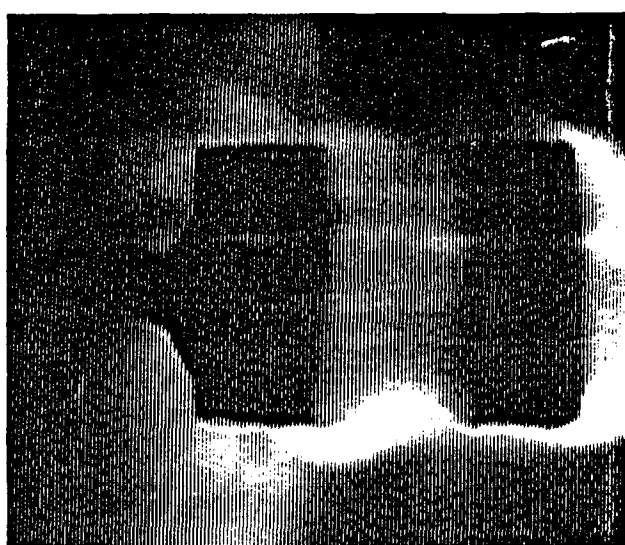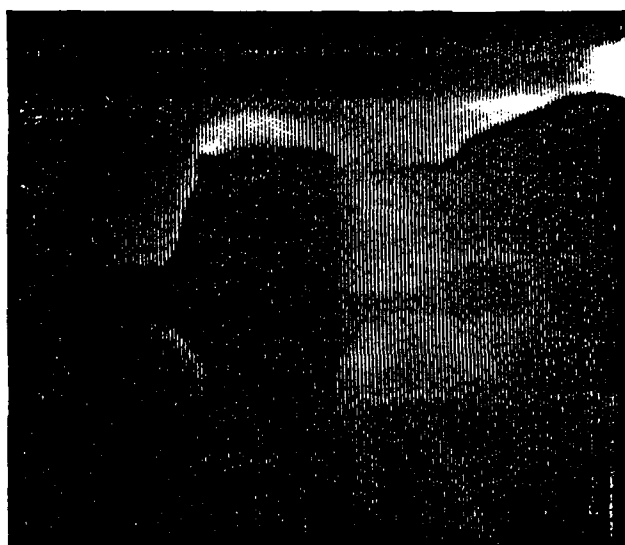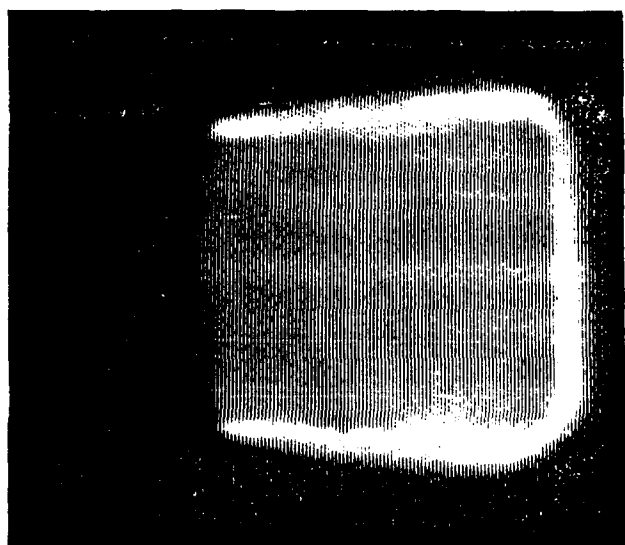Figure 15. Li Solid-SF$_6$ Combustion at 0.01 MPa

Figure 16. Li-SF$_6$ Wick Combustion at 0.01 MPa

achieved, the flame sustained itself until the wick was burnt out. During combustion the chamber interior showed a glowing pinkish color. A bright pinkish flame around the wick was recorded in the video tape. The aperture of the video camera was partially closed. Immediately after ignition, the flame spread over the wick surface and dark spots inside the luminous flame were observed. The flame then covered the side (wick) and bottom (cap) surfaces of the cylinder, showing a "uniform" flame (bright) surface. The flame surface (bright luminous layer) appeared quite close to the wick surface, the stand-off distance was only a few mm away from the wick surface. Near burn out, local extinction first appeared at the bottom surface and the upper portion of the wick. The extinction of the flame at the upper wick surface probably was a result of non-wetted wick surface near "complete consumption" of lithium fuel. Shortly after local extinction at the upper wick surface, the wick was burned out.

4.2 Theoretical Results

Ethanol-Air Wick Diffusion Flame. The conserved scalar approach yields a single equation for the interface condition, Eq. (17), dictated by the flame structure. One immediate observation is that the interface fuel vapor mass fraction is less than one under normal condition. This can be seen as the fuel vapor mass fraction decreases and the temperature increases as Z is decreased (or moving away from the interface). It is noted that the interface fuel vapor mass fraction may approach unity near the mixture thermodynamic critical point. Two system pressures, 0.03 and 0.1 MPa, were considered for ethanol-air wick combustion. The interface temperatures were determined 310 K and 336 K and the interface fuel vapor mass fractions were 0.6289 and 0.6382 for 0.03 and 0.1 MPa, respectively. The interface condition was obtained employing an iterative procedure to solve Eq. (17). Up to ten iterations were required for the two pressures considered. The state relationships of ethanol-air wick diffusion flames at 0.03 MPa and 0.1 MPa were illustrated in Figs. 17 and 18, respectively. The higher flame temperature at 0.1 MPa is a result of the equilibrium shift due to reduced dissociation at higher pressures.
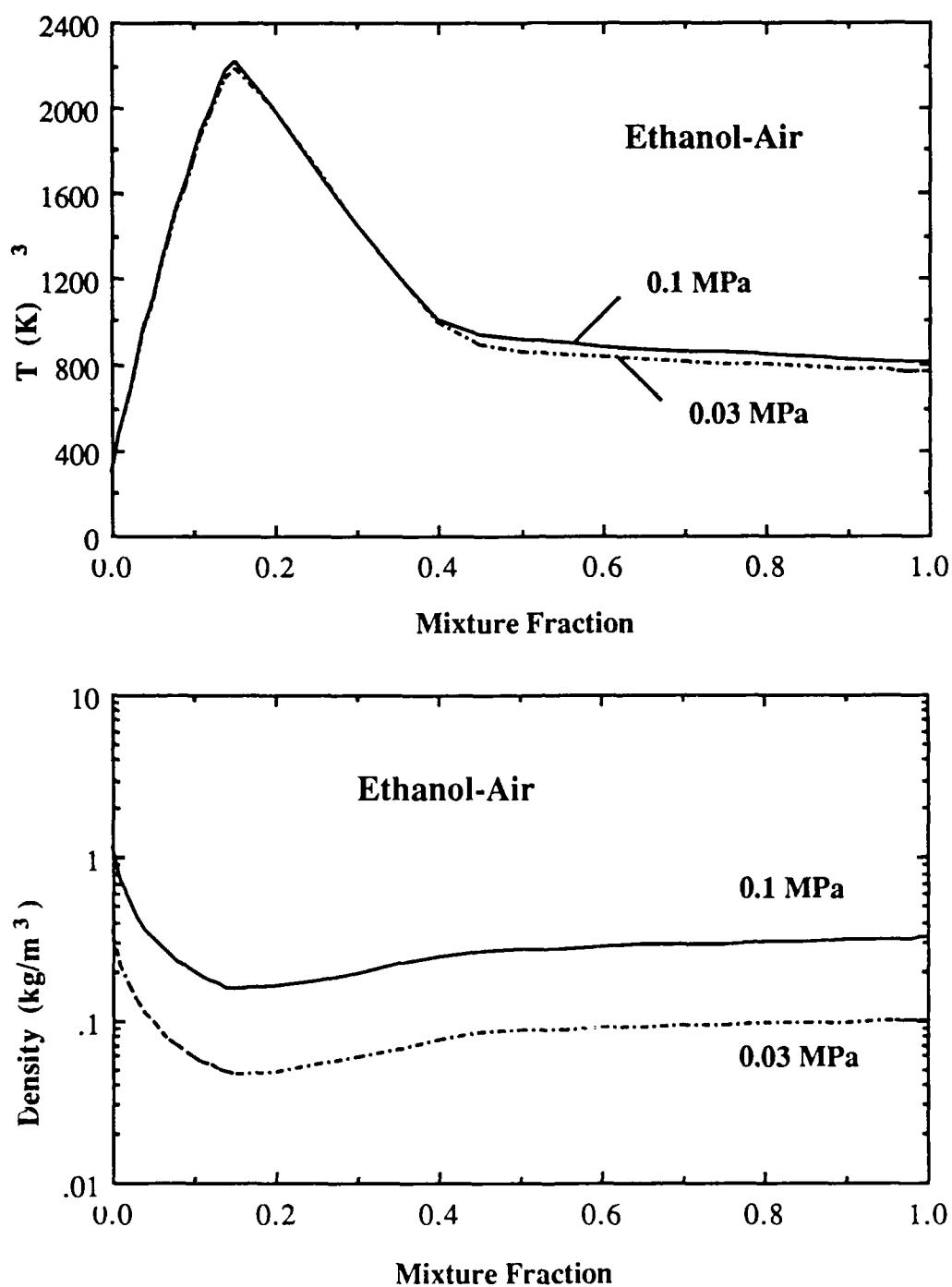
Figure 17. State Relationship (Temperature and Density) of Ethanol-Air Wick Diffusion Flame
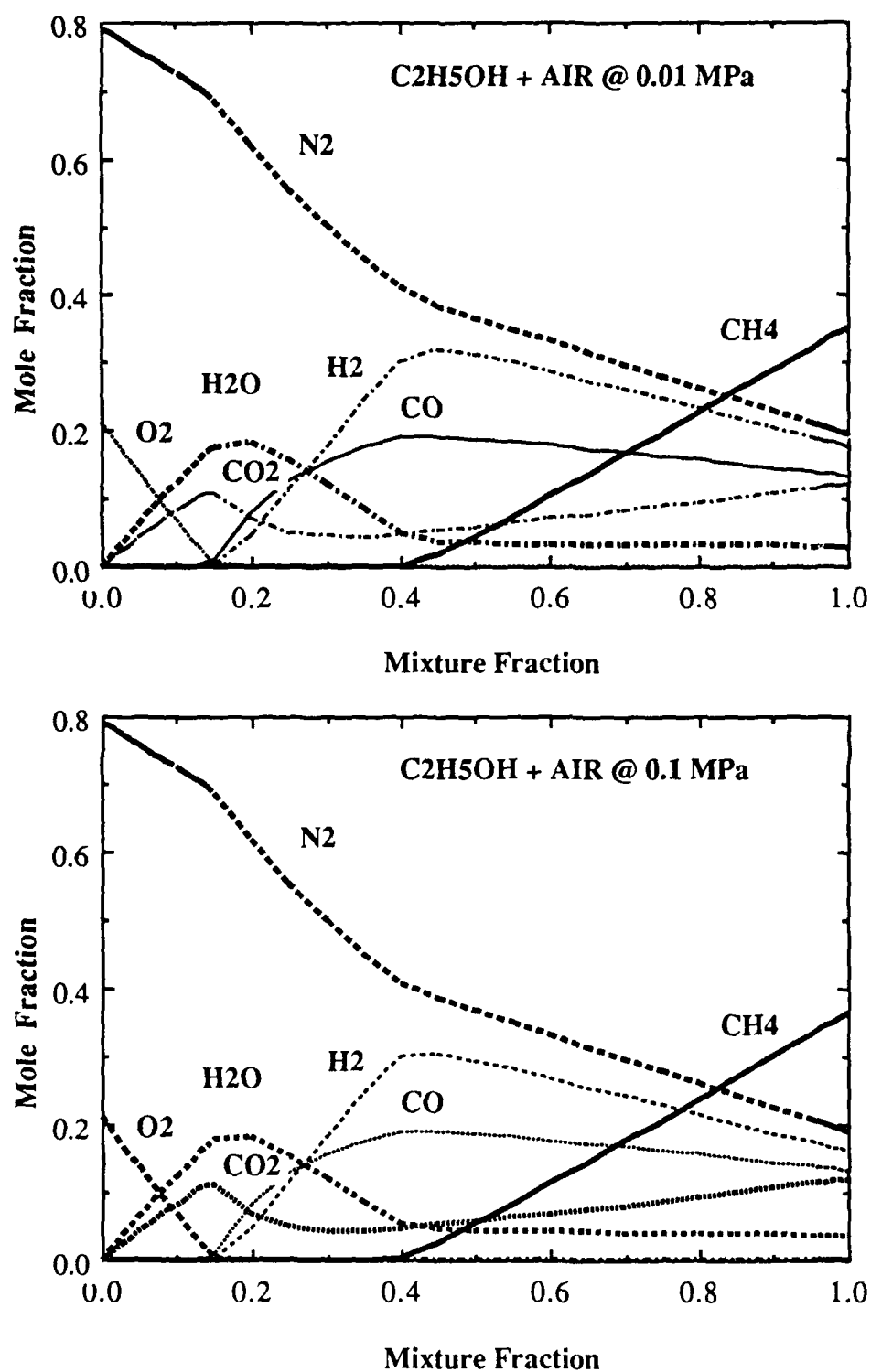
Figure 18. State Relationship (Concentration) of Ethanol-Air Wick Diffusion

Flame

In the computation reported herein, a flat-plate 100 mm wick was considered. The computation showed that similarity solutions were maintained for the conditions examined although non-similar governing equations were retained in the analysis. The solution yields similar profiles for f, f', f", Z and Z' at different streamwise locations when similarity variables were employed. The calculated mass burning rates yields a $\xi^{-0.25}$ dependence, typical of laminar boundary layer diffusion flames. The calculated mass burning rates are illustrated in Fig. 19. The predicted mass burning rates also showed a pressure dependence of $p.^{0.64}$

To illustrate the pressure effects on the flame stand-off distance from the wick surface, the predicted temperature and streamwise velocity profiles at the trailing edge of the 100 mm wick were shown in Fig. 20. As shown in the figure, the stand-off distance increased as the system pressure was decreased. This is in qualitative agreement with the experiments conducted, although the analysis over-estimated the stand-off distance by 50 %. The maximum streamwise velocities are comparable for the two pressures considered, with a higher maximum velocity at 0.1 MPa. This is not surprising as the momentum source term in dimensionless form is similar for the two pressures considered.

Li-SF6 Wick Diffusion Flame. Equilibrium computation was made to estimate the flame structure of the wick combustion, to estimate the pressure effects on wick combustion and to estimate the fuel composition effects on lithium combustion. The state relationships of Li-SF$_6$ wick flame at 0.01 and 0.1 MPa, assuming $Y_{Li} = 1$ at the interface, are illustrated in Figs. 21-23. At the interface (Z = 1), the fuel vapor was set at 1339 K and 1609 K (saturation temperatures) for 0.01 and 0.1 MPa, respectively. The equilibrium computation yields similar state relationships for 0.01 and 0.1 MPa. The 0.1 MPa case, however, has a higher temperature (4360 K versus 3884 K at 0.01 MPa) and a higher density as shown in Fig. 20. Fuel vapor was the major species at Z ≈ 1 either as lithium atoms (Li) or lithium dimers (Li$_2$), e.g. see Figs. 22 and 23. The oxidant appeared as SF$_6$ or SF$_4$ at Z ≈ 0; however, SF$_6$ decreased but SF$_4$ increased as Z increased from zero. From the equilibrium prediction, LiF is the major combustion product. Gas-phase LiF
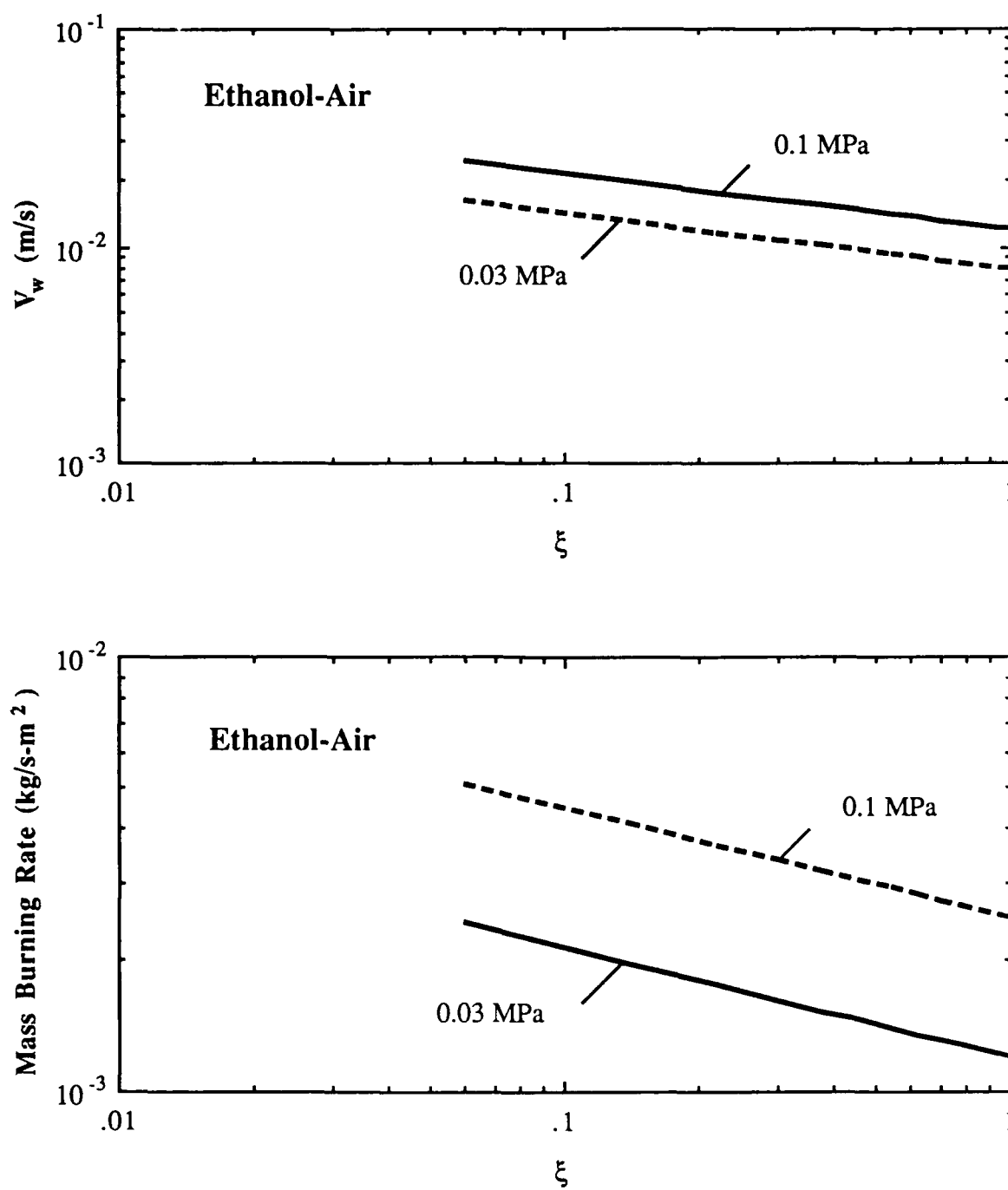
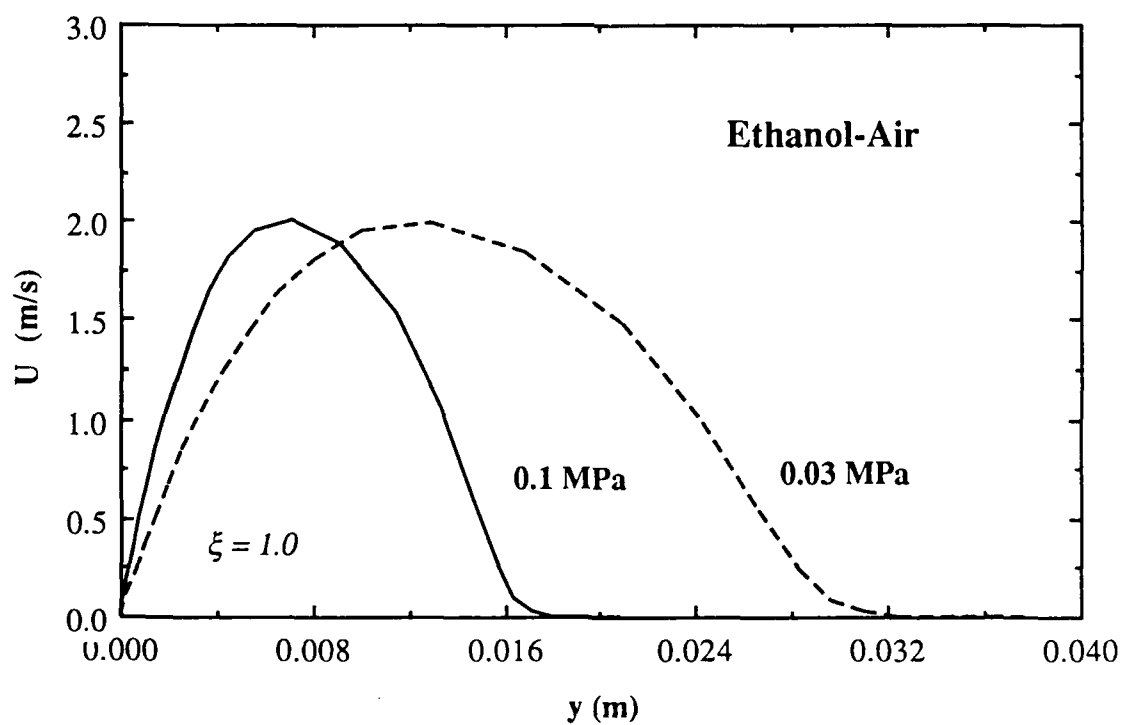Figure 19. Predicted v_w and $\dot{m}''$ of Ethanol-Air Wick Diffusion Flames
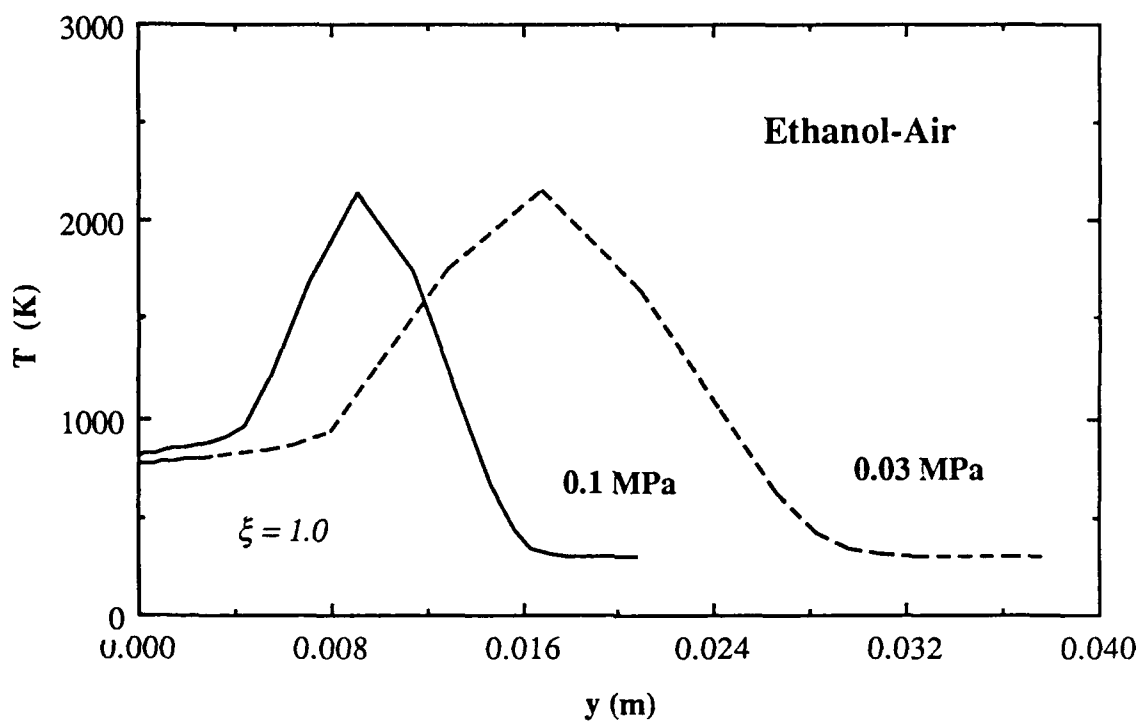
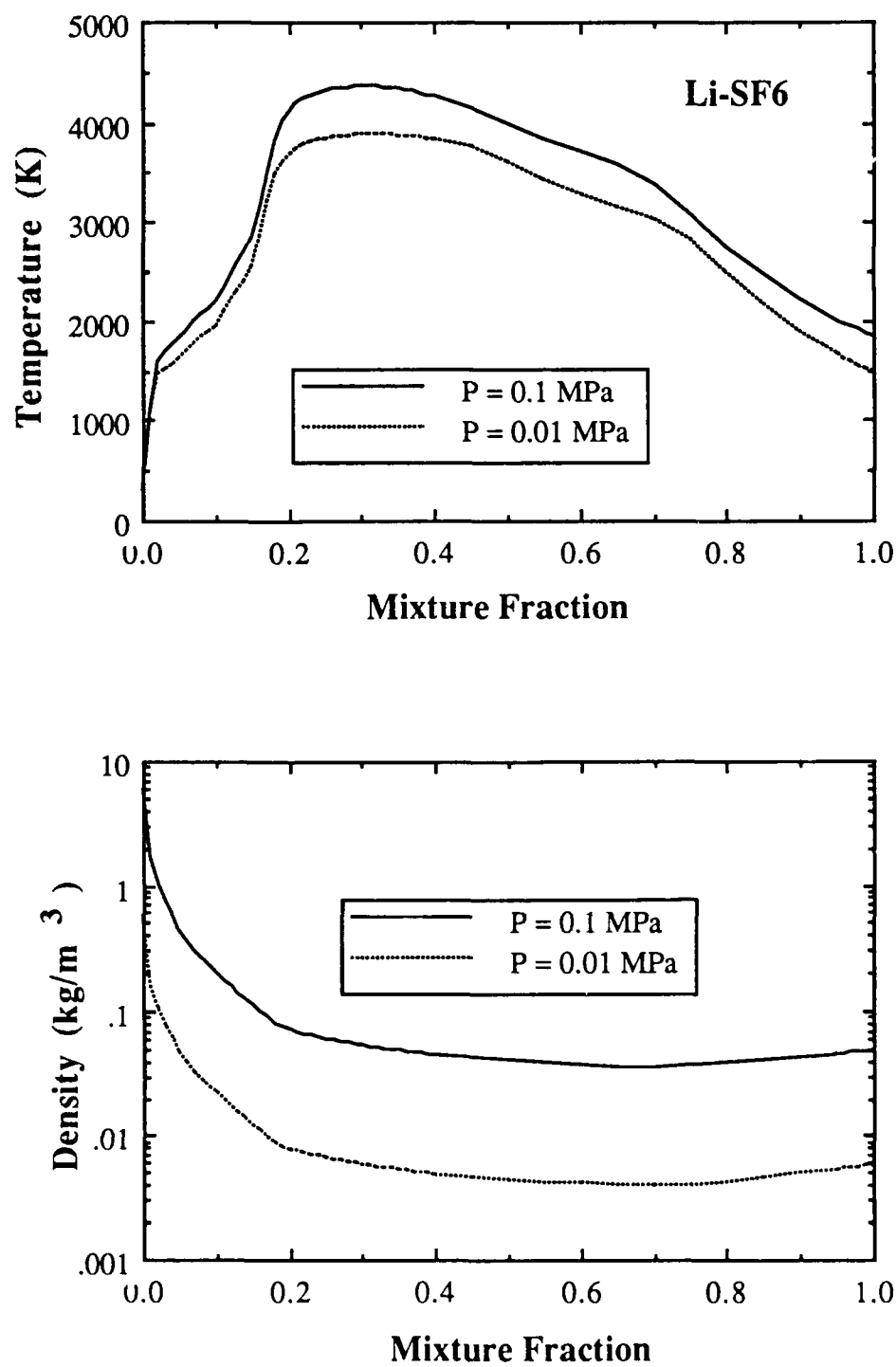Figure 20. Predicted Flame Structure of Ethanol-Air Wick Diffusion Flames

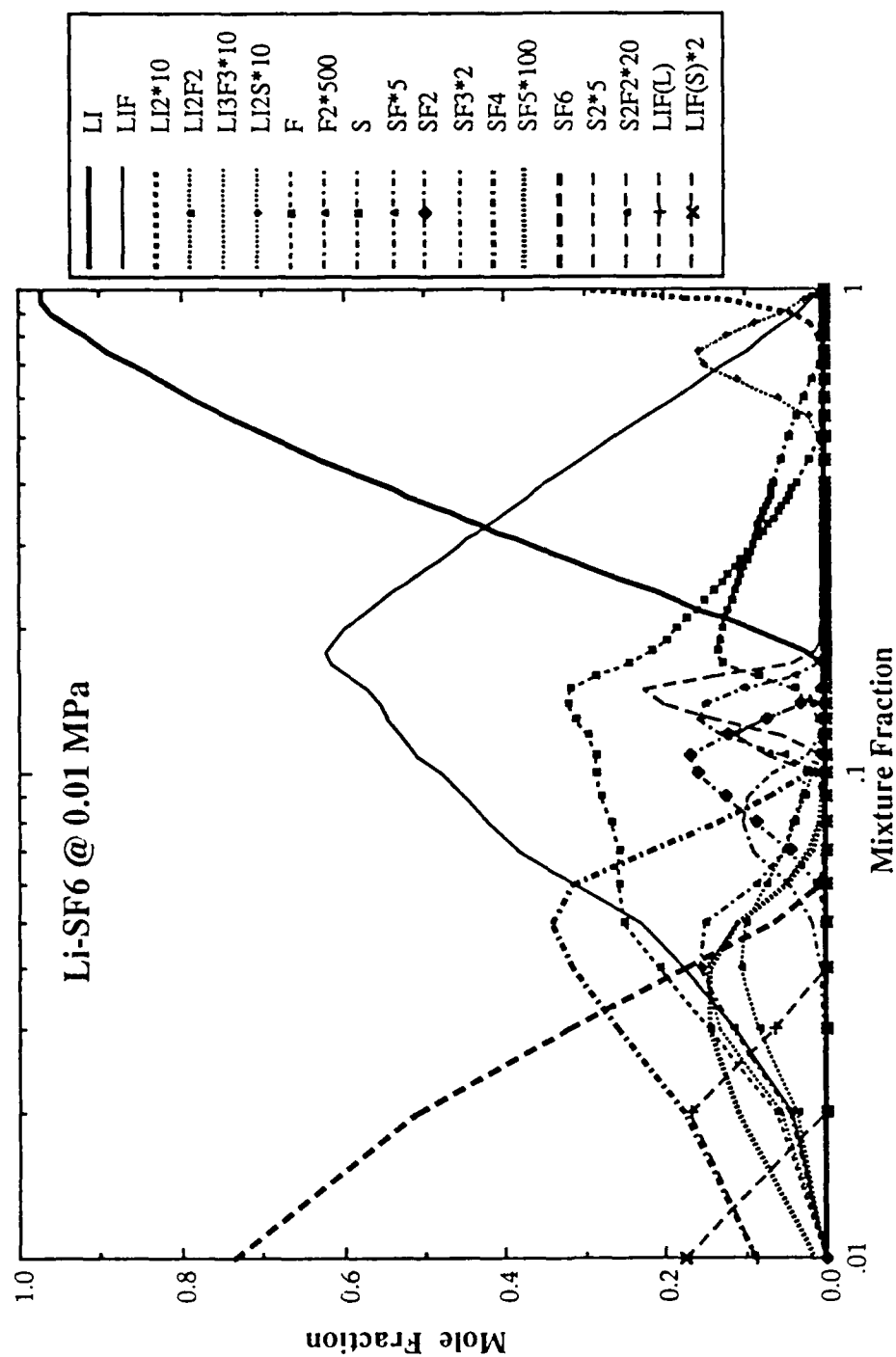Figure 21. State Relationship of Density and Temperature of Li-SF$_6$ Wick

Combustion

Figure 22. State Relationship of Species Concentration of Li-SF$_6$ Wick Combustion at 0.01 MPa
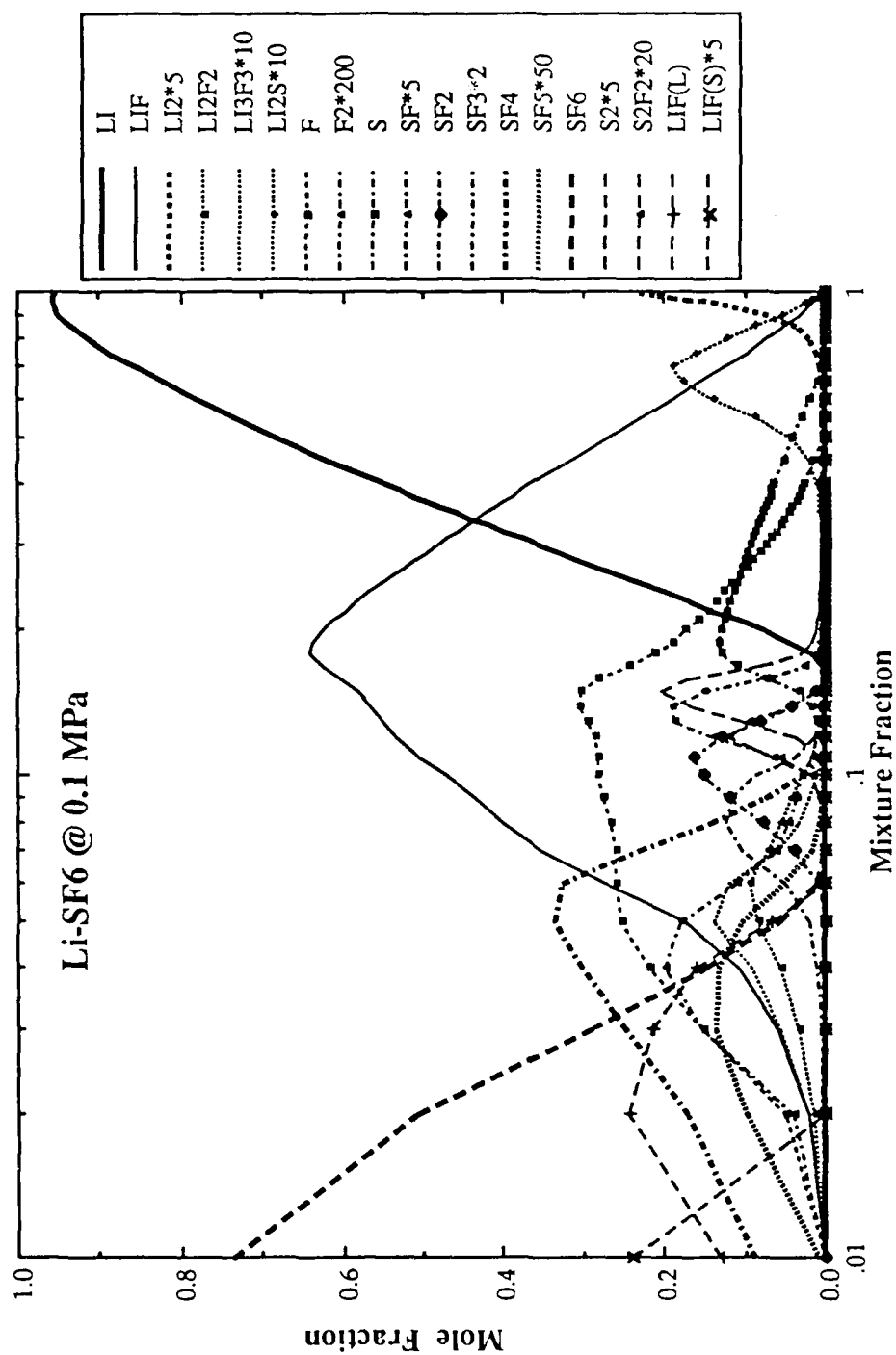
Figure 23. State Relationship of Species Concentration of Li-SF$_6$ Wick Combustion at 0.1 MPa

appeared over much of the mixture fraction space while liquid- and solid-phase LiF appeared in the oxidant rich regime. Only gaseous Li_2S in the fuel rich regime was predicted from the equilibrium calculation. The S species appeared as elemental sulfur (S) or SF_x (x = 1, 2, .., or 6) in the oxidant-rich regime.

The flowfield solution of Li-SF_6 wick combustion at 0.01 and 0.1 MPa was summarized in Figs. 24 and 25, employing the state relationships shown in Fig. 21. Similar to ethanol-air wick combustion, the prediction showed that similarity profiles prevailed in the flow. For example, nearly identical mixture fraction profiles (Z) and dimensionless velocity (f') were found at different streamwise locations, cf. Figs. 24 and 25. The pressure was also found to have negligible effects on predicted mixture fraction and dimensionless velocity profiles as one compared the results of 0.01 MPa and 0.1 MPa. The peak dimensionless velocity appeared at $\eta \approx 1$, corresponding to the maximum temperature location at which $Z \approx 0.3$. The lower pressure condition, i.e. 0.01 MPa, has a higher maximum dimensionless velocity (f' $\approx$ 0.40) than the 0.1 MPa condition (f' $\approx$ 0.38). The streamwise flow development was summarized in Figs. 26 and 27. The maximum streamwise velocity increased from 3.8 m/s at ξ = 0.22 (x = 0.022 m) to 8.1 m/s at ξ = 1 (x = 0.1 m) for the condition at 0.01 MPa while the maximum velocity increased from 4.0 m/s (ξ = 0.22) to 8.5 m/s (ξ = 1.0) for the condition at 0.1 MPa.; it is note that the 0.1 MPa condition had a lower maximum dimensionless velocity (cf. Fig. 25).

The boundary layer thickness grows in the streamwise direction, roughly following a $x^{0.25}$ dependence similar to that expected for natural convection laminar boundary layer flows. The flame stand-off distance increased as the system pressure was decreased; for example, the stand-off distance at 0.01 MPa was predicted three to four times the value at 0.1 MPa, cf. Figs. 26 and 27. The stand-off distance, however, remained constant over the entire plate in the transformed domain. This confirms the proper similarity transformation used in the analysis. The local wall blowing velocity due to gasification of the liquid was shown in Fig. 28 and the local fuel mass burning rate per unit surface area was summarized in Fig. 29. The wall blowing velocity (v_w) was

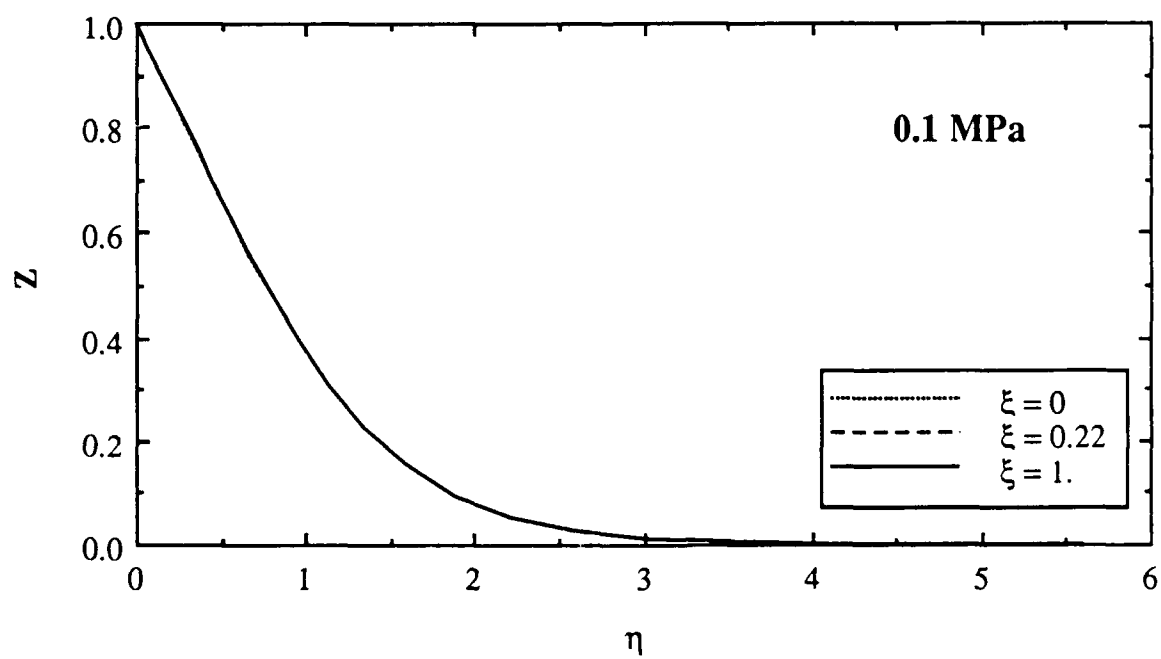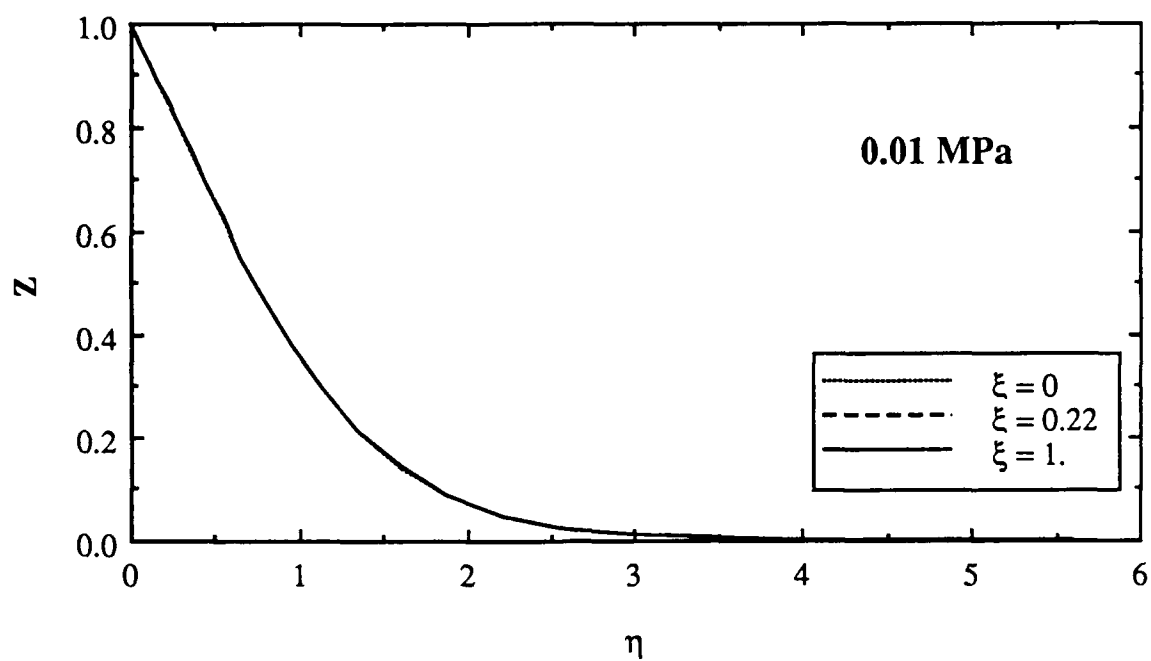Figure 24. Similarity Mixture Fraction Profiles of Li-SF$_6$ Wick Combustion
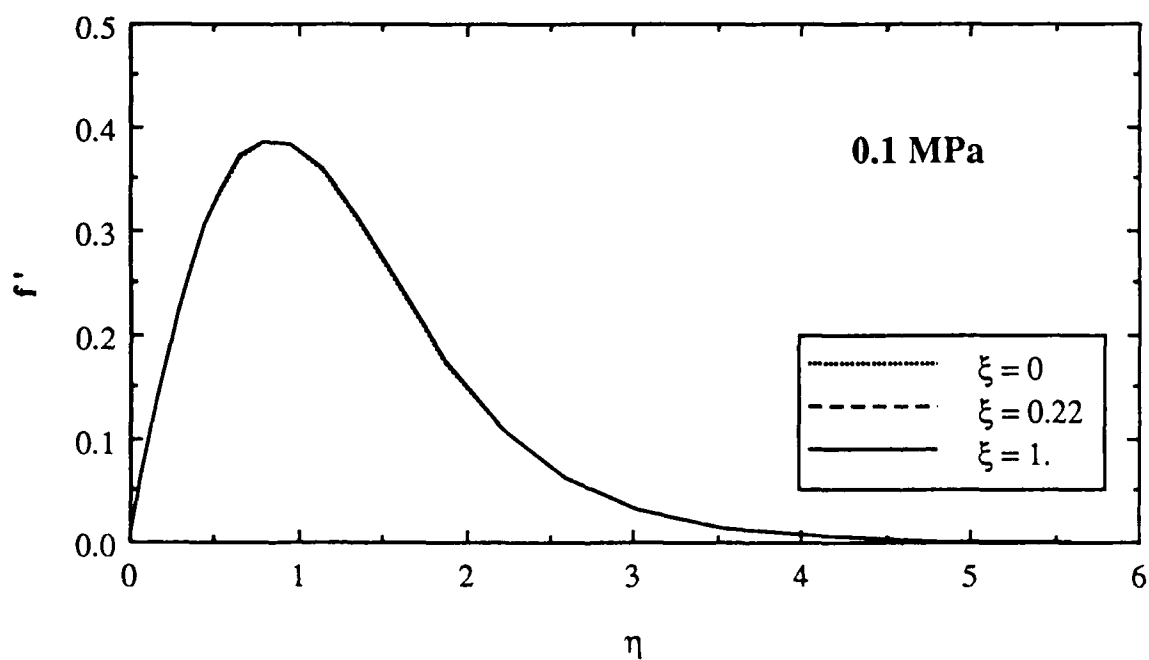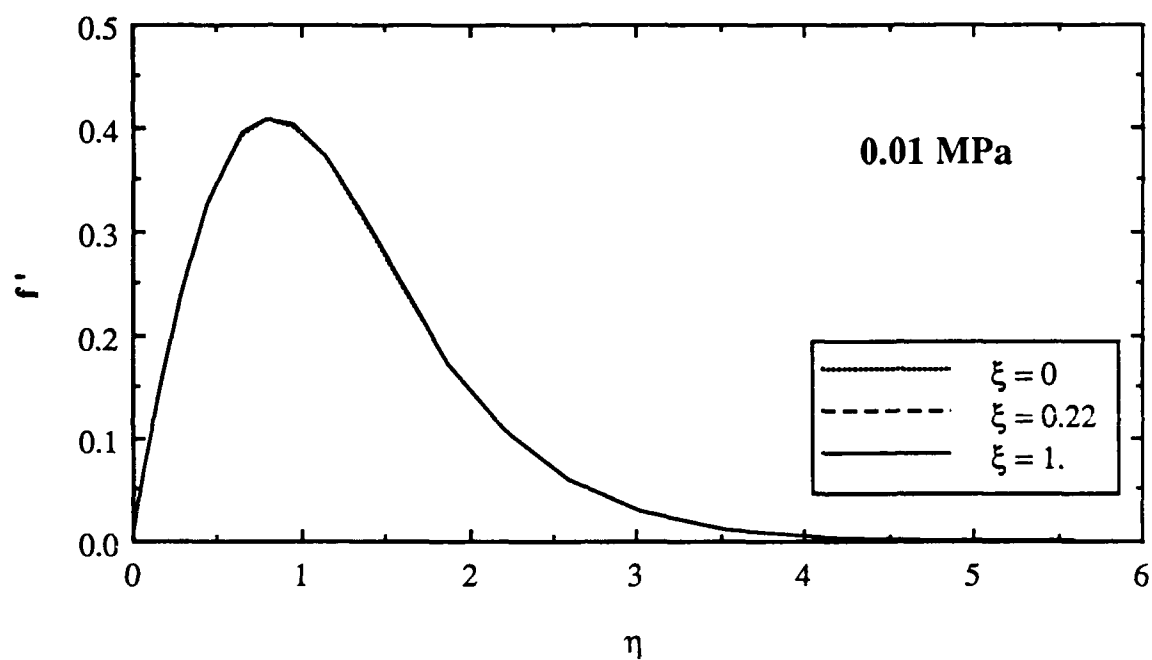
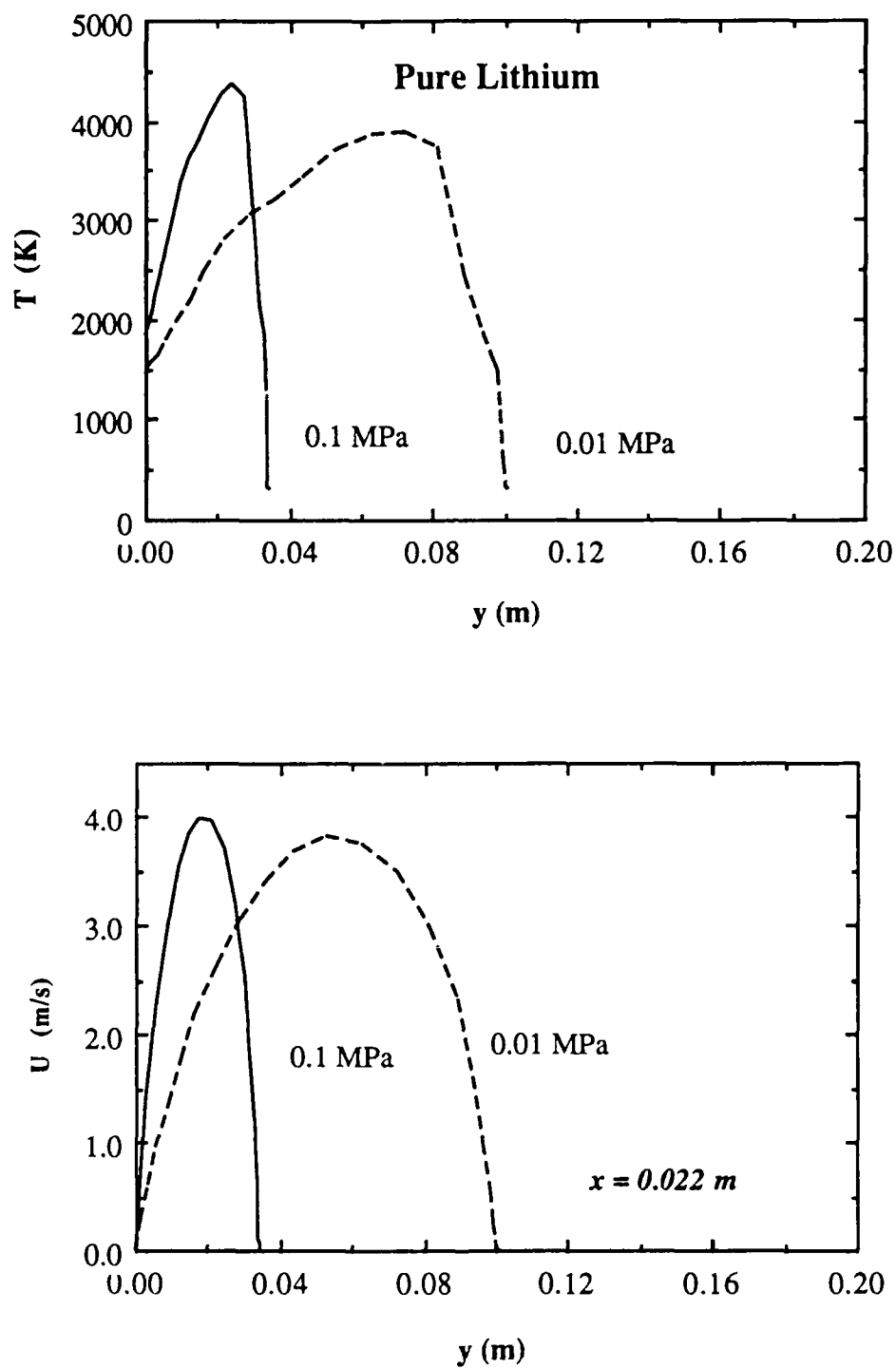Figure 25. Similarity Velocity Profiles of Li-SF$_6$ Wick Combustion

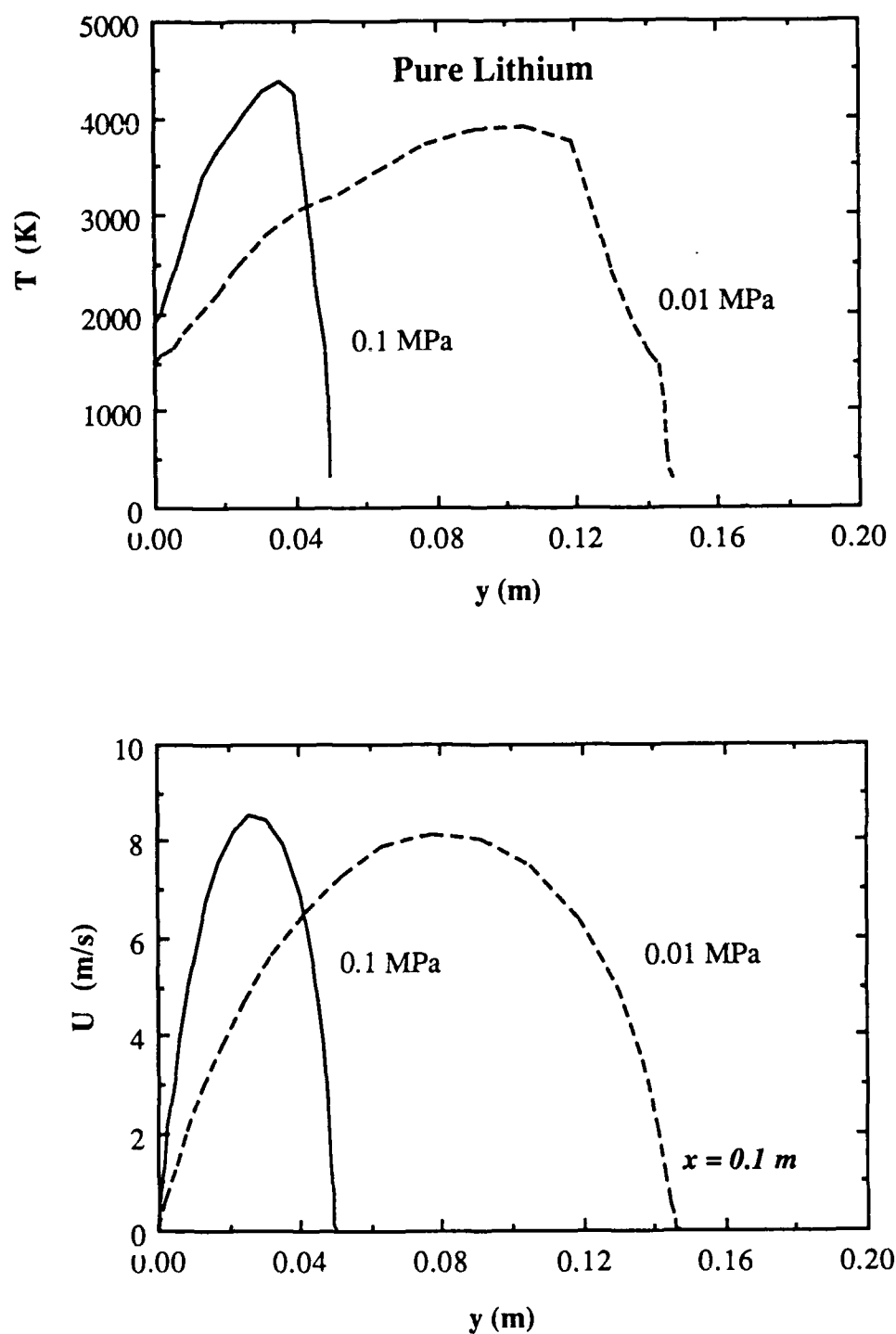Figure 26. Temperature and Velocity Profiles of Li-SF$_6$ Wick Combustion at $\xi = 0.22$

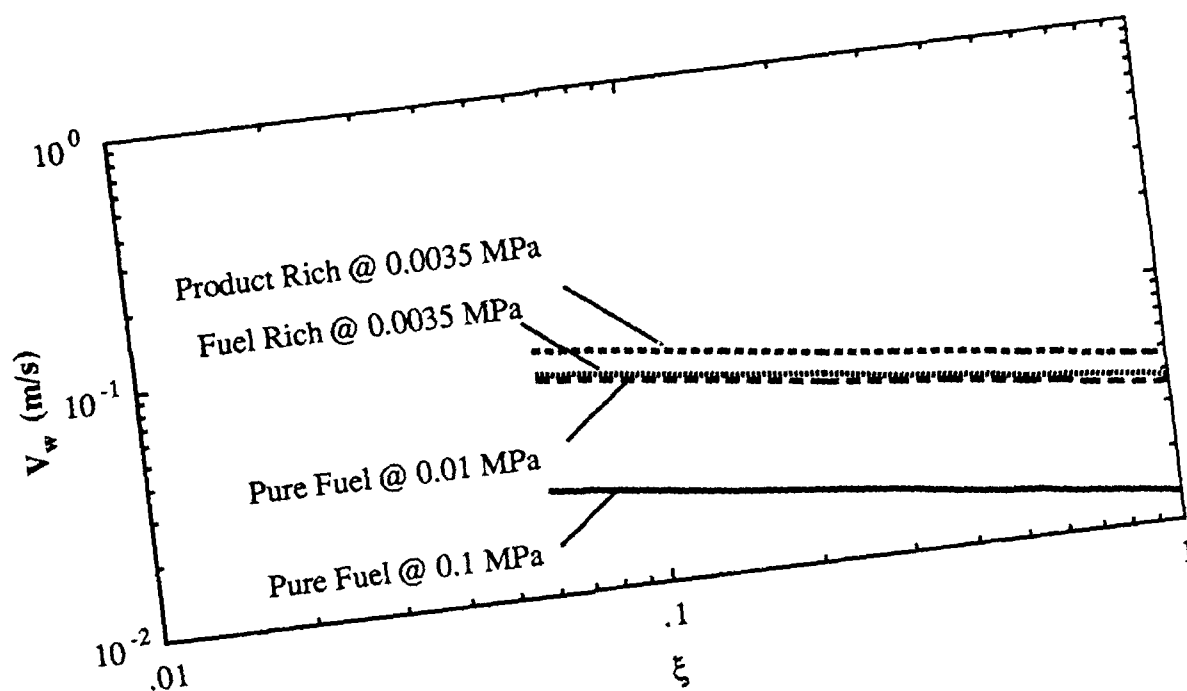Figure 27. Temperature and Velocity Profiles of Li-SF$_6$ Wick Combustion at $\xi = 1$

Figure 28. Local Wall Blowing Velocity
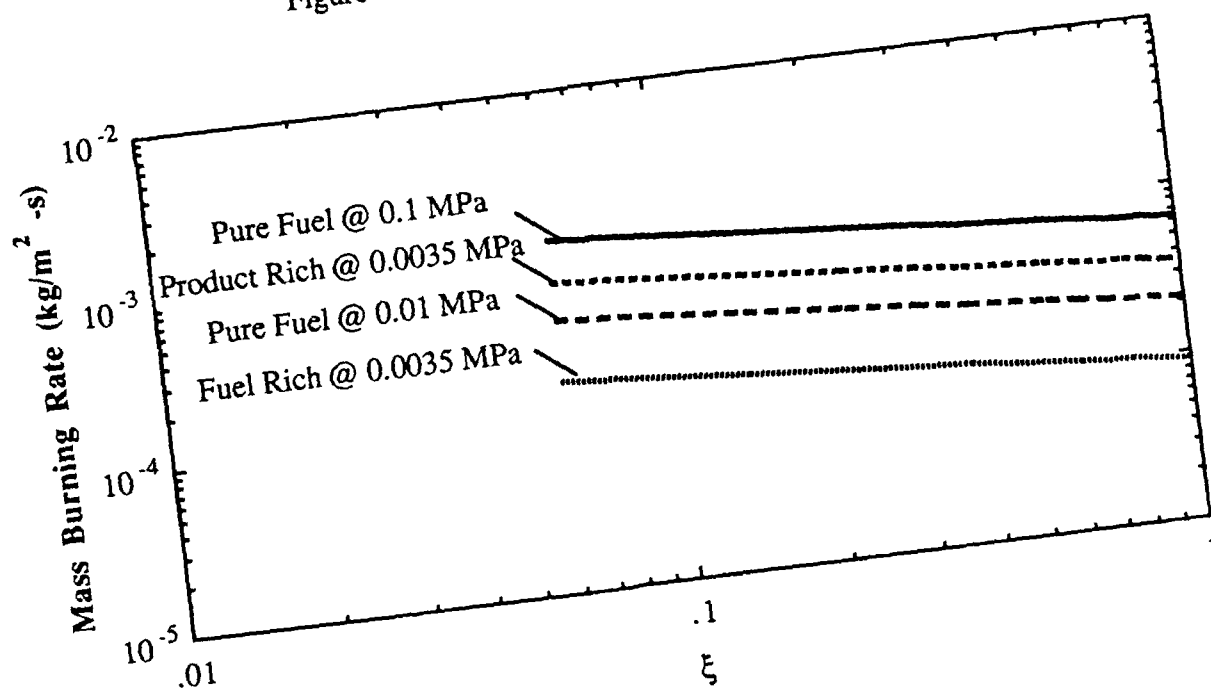

Figure 29. Local Fuel Mass Burning Rate

determined from Eq. (18) and the fuel mass burning rate ($\dot{m}''$) was obtained by multiplying v_w with local gas density. Both v_w and $\dot{m}''$ revealed a $x^{-0.25}$ dependence, similar to the results obtained for ethanol-air wick diffusion flames, in agreement with the classical results of heat and mass transfer in natural convection laminar boundary layer flows.

Also shown in Figs. 28 and 29 are the results based on the equilibrium properties of fuel-rich and product-rich liquids as fuel. The species composition of the fuel was taken from Groff and Faeth (1978a) for the condition at 0.0035 MPa (1250 K), e.g. see Fig. 30. The enthalpy of gasification was estimated assuming an ideal solution at its proper composition. The predicted mass burning rate decreased as the system pressure was decreased when pure lithium and fuel-rich liquids were considered; it is, however, quite surprising to note that the product-rich condition at 0.0035 MPa yields a mass burning rate higher than that of the fuel-rich condition at 0.0035 MPa and that of pure lithium at 0.01 MPa (cf. Fig. 29). The higher mass burning rate is a result of the increased heat transfer from the flame to the wick surface as the flame stand-off distance decreases when the initial Li mass fraction was decreased. The higher mass burning rate is also a result of reduced enthalpy of gasification per unit mass of the liquid, e.g. 21228 kJ/kg for pure Li 1609 K, 21950 for pure Li at 1339 K, and 21631 kJ/kg for pure Li, 19572 kJ/kg for fuel-rich liquid and 8381 kJ/kg for product-rich liquid at 1250 K. The higher mass burning rate does not imply a higher Li consumption rate since only little Li was present in the product-rich fuel. The results, however, suggest that the wick configuration may have the potential to achieve a higher fuel utilization than the submerged jet operation.
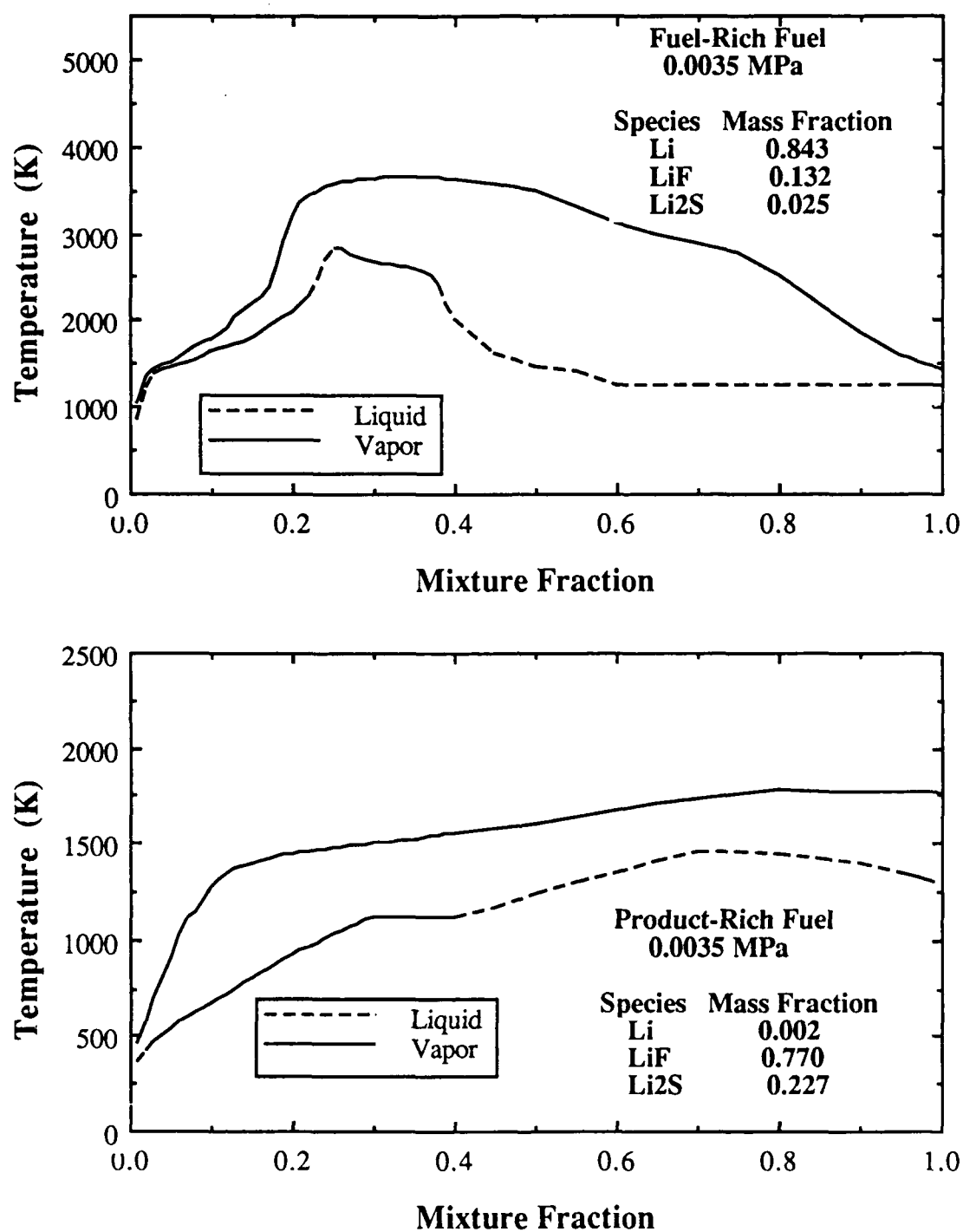
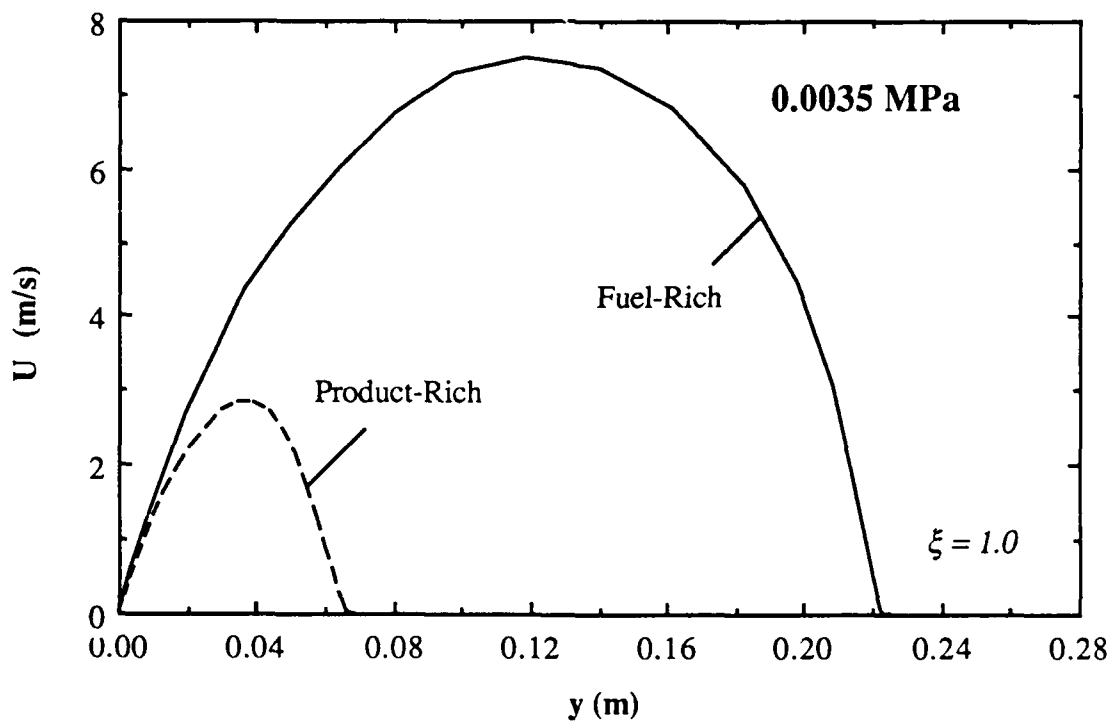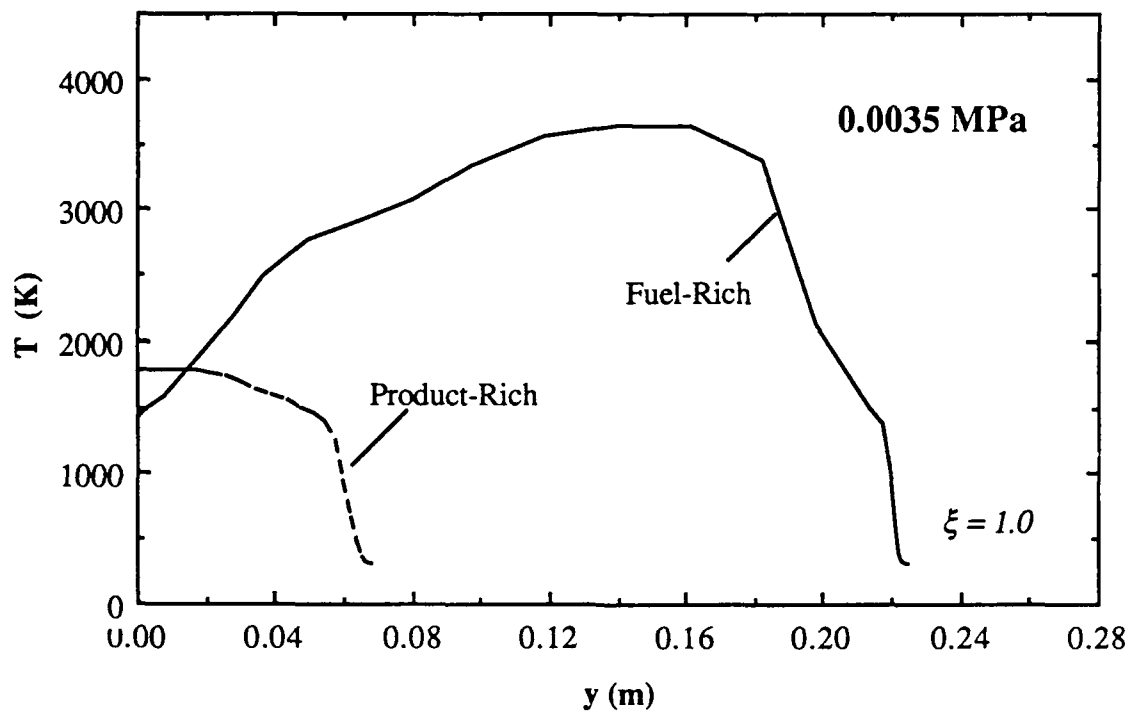Figure 30. State Relationship of Fuel-Rich and Product Rich Fuels

Figure 31. Li-SF$_6$ Wick Combustion of Fuel-Rich and Product-Rich Fuel at 0.0035 MPa.

V. SUMMARY AND FUTURE WORK

An experimental and theoretical investigation was conducted to study wick combustion of Li-SF$_6$. A single-line laser induced fluorescence thermometry technique with Li$_2$ as fluorescence species was developed and calibration experiments showed promising results with refinements identified for further development. Wick combustion of ethanol and hexane in air as well as Li and SF$_6$ was conducted in a vacuum chamber at atmospheric and sub-atmospheric pressures. The ethanol and hexane wick diffusion flames showed flame oscillations, similar to flame flickers in buoyant jet diffusion flames. The oscillation frequency was estimated in the range 5 to 8 Hz at the pressures examined. The flame stand-off distance was found to increase when the system pressure was decreased. The wick combustion of Li and SF$_6$ resulted in a bright pinkish flame. The luminous zone appeared quite close to the wick surface at the condition examined. Near the "complete consumption" of lithium, the wick was burned out due to loss of lithium as a heat sink.

On the analysis, a conserved scalar approach was employed to model the wick flame. A single equation was obtain to describe the interface condition of wick combustion. Numerical solutions were obtained for laminar wick diffusion flames. The prediction yields similarity profiles for both ethanol-air and Li-SF$_6$ wick diffusion flames although non-similar governing equations were retained in the formulation. The flame stand-off distance was found to increase as the system pressure was reduced, in agreement with theoretical predictions. The effects on mass burning rates due to varying fuel composition were studied employing the fuel-rich and product-rich liquids at 0.0035 MPa in the analysis. It was found the product-rich fuel yields a much lower flame temperature but the mass burning rates was not decreased. This is a result of the decrease in the flame stand-off distance, yielding an increase in heat transfer to the wick surface, as well as the reduced specific enthalpy of gasification when a product-rich liquid was used. In fact, the mass burning rates were higher than the fuel-rich fuel at the same pressure and even higher than the pure lithium at 0.01 MPa. The findings on fuel mass burning rates are interesting since it suggests that the wick configuration may achieve a higher fuel utilization than the submerged jet.

Work is in progress to document the spectroscopy of Li-SF_6 wick diffusion flames and to include the curvature effects in modeling wick combustion. It should be noted that the spectroscopy data of Li and SF_6 combustion are not presently available in the literature. The current work represents the first experimental effort to obtain such data. The inclusion of curvature in the modeling will clarify its effects on fuel mass burning rates and on the transport processes. The wick flames were found to exhibit spatial and temporal periodicities in ethanol and hexane diffusion flames and time dependent burning of Li in SF_6. The modeling will be extended to include the time dependent effects and the experiments will be made for time-dependent Li mass burning rate measurements. In quantifying the thermochemical properties of Li and SF_6 combustion, the feasibility of LIF with LiF as the fluorescence species will be explored. This is due to that the signal to noise ratio of Li_2 LIF may be deteriorated in the combustion environment as a result of the strong luminosity observed in the experiments. Thus it is desired to use the major combustion product, LiF, as the fluorescence species.

New laser diagnostics will also be employed in the next year's experiments; for example, a gated image intensified (IIT F4111 Intensifier Tube and Power Supply @ 180 ns shutter opening) CCD Camera (Photometrics/Thomson CSF TH7882CDA CCD; 576 x 384 Pixels) will be used for planar imaging of the wick Li-SF_6 combustion. Due to the strong flame luminosity, the frequency doubled second harmonic output of a Nd:YAG laser (Spectra Physics GCR-4-10 Nd:YAG Laser and PDL-3 Dye Laser) will be used as the uv source for Mie scattering imaging of the flame. The Nd:YAG laser and the pulsed dye laser will be explored as the excitation laser source for LIF thermometry. The planar Mie scattering of the wick Li-SF_6 flame should shed some light on if there exist condensed-phase products in the fuel rich regime. The Nd:YAG laser is also equipped with a double pulse option which can be used to develop particle tracking velocimetry to characterize the hydrodynamic aspects of the flame. The new diagnostics will add an additional dimension to quantify thermochemical properties and hydrodynamic characteristics of the wick combustion of Li and SF_6, providing a better understanding of the combustion process.

REFERENCES

Alstadt, R. H. and Faeth, G. M., 1977, "An Investigation of Wick-Type Metal Combustors," Technical Report to DARPA (DARPA Contract No. N00600-74-C-0033), The Pennsylvania State University.

Avery, J. F. and Faeth, G. M., 1975, "Combustion of a Submerged Gaseous Oxidizer Jet in a Liquid Metal", *15th Symp. Combust.(International)*, The Combustion Institute, pp. 501-512.

Bilger, R. W., 1980, "Turbulent Flows with Non-premixed Reactants", in *Turbulent Reacting Flows* (P. A. Libby and F. A. Williams, Ed.), Springer-Verlag, pp. 65-114.

Blakeslee, T. R., 1977, "Laminar Free-Convective Combustion of a Liquid Metal from a Wick", Ph.D. dissertation, The Pennsylvania State University.

Chase, M. W., Jr., Davies, C. A. Downey, J. R., Jr., Frurip, D. J., McDonald, R. A. and Syverud, 1985, *JANAF Thermochemical Tables*, 3rd Ed., Part I and II, ACS/AIP.

Chen, L.-D. and Faeth, G. M., 1981, "Ignition of a Combustible Gas along Heated Vertical Surfaces", *Combust. Flame*, Vol. 42, pp. 77-92.

Chen, L.-D. and Faeth, G. M., 1982, "Ignition of Supercritical Fluids During Natural Convection from a Heated Vertical Surface," *Combust. Flame*, Vol. 44, pp. 169-183.

Chen, L.-D. and Faeth, G. M., 1983, "Structure of Turbulent Reacting Gas Jets Submerged in Liquid Metals", *Combust. Sci. Technol.*, Vol. 31, pp. 277-296.

Colodner, P., Winterfield, C., and Yabionovitch, Y., 1977, *Opt. Commun.*, Vol. 20, p. 119.

Faeth, G. M., Groff, E. G., You, H-Z., Alstadt, R., and Icenhower, D., 1978, "A Reactive-Heat-Pipe for Combined Heat Generation and Transport", *Proceedings of 3rd International Heat Pipe Conference*, Palo Alto, CA, 22-24 May 1978.

Flower, W. L. and Bowan, C. T., 1984, "Measurements of The Structures of Sooting Laminar Diffusion Flames at Elevated Pressures", *20th Symp. Combust.(International)*, The Combustion Institute, pp. 1035-1044..

Gordon, S. and McBride, B. J., 1976, "Computer Program for Calculation of Complex Chemical Equilibrium," NASA SP-273, NASA.

Ginzburg, I. P., Surin, V. A., Bagautdinov, A. A., Grigor'yants, A. S., and Shub, L. I., 1977, "Study of the Discharge Process into a Liquid of a Gas Stream from an Immersed Nozzle", *J. Engineering Physics*, Vol. 33, pp. 879-887.

Groff, E. G., 1976, "Characteristics of a Steadily Operating Metal Combustor," Ph. D. Dissertation, Pennsylvania State University.

Groff, E. G. and Faeth, G. M., 1978a, "Phase Equilibria in the Li-LiF-Li$_2$S Systems", *Ind. Eng. Chem. Fundam.*, Vol. 17, pp. 326-330.

Groff, E. G. and Faeth, G. M., 1978b, "Steady Metal Combustor as a Closed Thermal Energy Source", *J. Hydronautics*, Vol. 12, pp. 63-70.

Hanson, R. K., 1987, "Combustion Diagnostics: Planar Imaging Techniques," *21st Symp. (Int.) Combust.*, The Combustion Institute, in press.

Hughes, T. G., Smith, R. B., and Kiley, D. H., 1983, "Stored Chemical Energy Propulsion Systems for Underwater Applications", *J. Energy*, Vol. 7, pp. 128-133.

Koch, M. E., Verma, K. K., Bahns, J. T., and Stwalley, W. C., 1983, "Laser-Induced Plasmas in Alkali Metal Vapors," in Proceedings on the International Conference on Lasers '82, (R. C. Powell, Ed.), STS Press, McLean, VA, pp. 119-123.

Laurendeau, N. M., 1987, "Temperature Measurements by Light-Scattering Methods," in *Developments in Experimental Techniques in Heat Transfer and Combustion* (R. O. Warrington, Jr., Ed.), ASME HTD-Vol. 71, pp. 45-65.

Lebedev, A. D. and Sokolov, A. S., 1985, "Features of Bubble Ignition and Combustion of Condensed Products," *Combust. Explosion and Shock Wave*, Vol. 21, pp. 393-398.

Lewis, G. N. and Randall, M, 1961, *Thermodynamics*, 2nd E., McGraw-Hill, pp. 242-279.

Loth, E. and Faeth, G. M., 1989, "Structure of Underexpanded Round Air Jets Submerged in Water," *International J. Multiphase Flow*, Vol. 15, No. 4, pp. 589-603.

Lucht, R.P., Sweeney, D.W., and Laurendeau, N.M., 1980, "Balanced Cross-rate Model for Saturated Molecular Fluorescence in Flames Using a Nanosecond Pulse Length Laser," *Appl. Opt.*, Vol. 19, pp.3295-3300.

Lucht, R.P., Laurendeau, N.M., and Sweeney, D.W., 1982, "Temperature Measurement by Two-line Laser-saturated OH Fluorescence in Flames", *Appl. Opt.*, Vol. 21, pp.3729-3735.

Mahaffy, J. H., 1986, in The First ONR Workshop on Closed Liquid Metal Combustion, 19-20 November 1986, University Park, Pennsylvania.

Maksimov, Yu. M., Kirdyashkin, A. I., Merzhanov, A. G., and Raskolenko, L. G., 1984, "Influence of Ultrasonic Vibrations of the Combustion of Condensed Systems with Solid-Phase Reaction Products," *Combust. Explosion and Shock Wave*, Vol. 20, pp. 669-672.

McBride, B. J. and Zeleznik, F. J., 1984 "Computer Program for Calculation of Complex Chemical Equilibrium Compositions and Applications Supplement I," NASA TM 86885, NASA.

Michel, A., "Thermohydraulic Applications of Liquid Metals in the Non-nuclear Field", in *Thermohydraulics of Liquid Metals*, Lecture Series 1983-07, von Karman Institute, Belgium, 1983.

Okhotskii, V. B., 1984, "Hydrodynamics of Interaction of a Gas Jet and a Liquid," *J. of Engineering Physics*, Vol. 47, pp. 550-558 (pp. 1140-1146, 1985, Plenum Publishing Corp.).

Pan, C.-Z, Bruzzese, R., Solimeno, S., and Velotta, R., 1987, "Interferometric Studies of Nonlinear Relaxation Processes in Vibrationally Highly Excited SF6 Molecules," *J. Opt. Soc. Am. B*, Vol. 4, pp. 452-461.

Parnell, L. A., 1987, in The Second ONR Workshop on Closed Liquid Metal Combustion, 14-15 October 1987, Pasadena, California.

Parnell, L. A., 1989, "Combustion Instabilities of Submerged Jets in Liquid Metal Fuels," AIAA/SAE/ASME/ASEE 25th Joint Propulsion Conference, July 10-13, 1989, Monterey, California, AIAA Paper No. 89-2825, AIAA.

Parsons, M. L., Smith, B. W., and Bentley, G. E., 1975, *Handbook of Flame Spectroscopy*, Plenum Press, NY, 1975.

Roquemore, W. M., Goss, L. P, Lynn, W. F., and Chen, L.-D., "A Study of the Structure of Jet Diffusion Flames," 1988 *AIAA Aerospace Sciences Meeting*, Reno, Nevada.

Salmon, J.T. and Laurendeau, N.M., 1985, "Analysis of Probe Volume Effects Associated with Laser-saturated Fluorescence Measurements", *Applied Optics*, Vol. 24, pp.1313-1321.

Simpson, M. E. and Chan, C. K., 1982, "Hydrodynamics of s Subsonic Vapor Jet in a Subcooled Liquid", *J. Heat Transfer*, Vol. 104, pp. 271-279.

Stunlinger, E., 1964, *Ion Propulsion for Space Flight*, McGraw-Hill, p. 185.

Stwalley, W.C. and Koch, M.E., 1980, "Alkali Metal Vapors: Laser Spectroscopy and Applications", *Opt. Engineering*, Vol. 19, pp. 71-83.

Sukhov, G. S. and Yarin, L. P., 1981, "Combustion of a Jet of Immiscible Fluids", *Combust. Explosion and Shock Wave*, Vol. 17, pp. 146-151.

Surin, V. A., Evchenko, V. N., and Rubin, V. M., 1983, "Propagation of a Gas Jet in a Liquid," *J. of Engineering Physics*, Vol. 45, pp. 542-554 (pp. 1091-1101, 1984, Plenum Publishing Corp.).

Tsuji, H, 1982, "Counterflow Diffusion Flames," *Prog. Energy and Combust Sci.*, Vol. 8, pp. 93-119.

Vargafitik, N. B., Kapitonov, V. M., and Voshchinin, A. A., 1985, "Experimental Study of the Thermal Conductivity of Lithium Vapor," *J. Engineering Physics*, Vol. 49, No. 4, pp. 634-639 (pp. 1208-1212, 1986, Plenum Publishing Corp.).

Verma, K. K., Koch, M. E., and Stwalley, W. C., 1983, "Observation of Levels near Dissociation in the $X^1\Sigma_g^+$ State of $^7Li_2$," *J. Chemical Physics*, Vol. 78, Part II, pp. 3614-3622.

Verma, K. K. and Stwalley, W. C., 1981, "Assignment of the $^7Li_2$ Optically Transitions Pumped by Ar+ and Kr+ Laser Lines," *J. Applied Physics*, Vol. 52, pp. 3821-3826.

Weimer, J. C., Faeth, G. M., and Olson, D. R., 1973, "Penetration of Vapor Jets in Subcooled Liquids", *AIChE J.*, Vol. 19, pp. 552-558.

Williams, F. A., 1985, *Combustion Theory*, 2nd Ed., Chapter 3, Benjamin/Cummings Publishing Co., pp. 38-91.

You, H-Z. and Faeth, G. M., 1977, "A Reactive-Heat-Pipe for Combined Heat Generation and Transport", Technical Report to DARPA (DARPA Contract No. N00600-74-C-0033), The Pennsylvania State University.